Alma Mater Studiorum – Università di Bologna

DOTTORATO DI RICERCA IN

INGEGNERIA ELETTRONICA, TELECOMUNICAZIONI
E TECNOLOGIE DELL'INFORMAZIONE

Ciclo XXIX

Settore Concorsuale di afferenza: 09/F1

Settore Scientifico disciplinare: ING-INF/02

ANALYSIS AND EXPLOITATION OF MULTIPLE ANTENNAS INTERACTION IN THE NEAR-FIELD

Presentata da: Francesco Berra

Coordinatore Dottorato

Prof. Alessandro Vanelli-Coralli

Supervisore

Prof.ssa Alessandra Costanzo

Co-Supervisore

Dott. Ing. Diego Masotti

Esame finale anno 2018

To last, to love, to life,

with smile.

Abstract

This thesis is structured in two parts. The former, and main one, introduces a novel solution for portable devices to exploit their existing communication antennas for bi-directional near-field wireless re-charging, without compromising their far-field properties. To demonstrate the concept, the GSM 900/1800 MHz and the 433 MHz, bands are adopted for the far-field communication and for the near-field wireless recharging, respectively. First, a pair of faced, dual-band, printed monopoles is characterized as a two-port network over all the bands of interest, by full-wave analysis, at several distances. Then, each antenna is fed by a frequency-selective three-port network, which is designed to simultaneously ensure data communication at the higher frequency bands and wireless re-charging at the lower frequency band. In this way, the combined far-field and near-field operations of the resulting four-port network can be optimized. Good performances are predicted in terms of ports isolation, power transfer efficiency and far-field radiation. As a proof-of-concept a system prototype is built: it ensures ports isolation higher than $20\,dB$, RF-to-RF power transfer efficiency ranging from 15% to 40%, with variable distance, in the $10 - 30\,mm$ range, between the faced antennas. When a rectifier is connected to the receiving power port, the measured RF-to-DC link efficiency, from the link input power port to the rectifier DC output, varies from 9% and 20% when the port-

able devices are located 1 and 2 centimetres apart, and the transmitted power is $10\,dBm$. This demonstrates that wireless charging and communication can be simultaneous with the proposed link arrangement and it can thus be used to exploit the charged state of an available device to recharge another one, without limiting the respective communication capabilities.

The latter part regards the activity I did as a visiting researcher at the Institute of Microwave and Photonic Engineering (IHF) at the Graz University of Technology (Graz, Austria) for my PhD period abroad. In particular, I worked on a fast design method for an RFID antenna, used as a transducer, to realize an RFID bent sensor tag. The method exploits a space mapping technique, using a coarse circuit model (CM) and a fine electromagnetic model (EM). The CM represents, in a CPU-time efficient way, the antenna transducer states to fast evaluate the sensor tag efficiency. The EM model is then used to verify the sensing states and to rapidly prototype the antenna. To demonstrate the procedure, the corresponding EM-based and CM input impedances of a T-matched dipole are compared for several sensing states; the maximum relative error between the CM model and the EM simulation is lower than 14% and 0.8%, for the antenna impedance real and imaginary parts, respectively. This is observed over a frequency band of 840-890 MHz. An innovative Figure of Merit has been introduced. This Figure of Merit has been exploited as the addressing function for an optimization algorithm implemented through the CM. Some design rules have been drown and explained in order to convert the CM optimization results into the EM ones. Finally the sensor tag efficiency is computed to compare the CM results with respect to the EM ones and in order to validate the entire space mapping technique.

Contents

List of Figures

List of Tables

Abbreviations

CC	Capacitive Coupling
CM	Circuit Model
CPT	Capacitive Power Transfer
DC	Direct Current
EM	Electromagnetic Model
FF	Far-Field
FFC	Far-Field Communication
IC	Integrated Circuit
IoT	Internet of Things
IPT	Inductive Power Transfer
LF	Low Frequency
NF	Near-Field
NFC	Near-Field Communication
PDA	Personal Digital Assistant
RF	Radio Frequency
RFID	Radio Frequency IDentification
RX	Receiver / Receiving
SMD	Surface Mount Device
SWIPT	Simultaneous Wireless Information and Power Transfer
TX	Transmitter / Transmitting
UHF	Ultra High Frequency

VNA	Vector Network Analyzer
WPT	Wireless Power Transfer

Introduction

With the increase of wireless applications and communications technologies exploiting several frequency bands, portable devices (PDA) are already equipped with complex antenna structures to comply with several wireless operations and there is an increasing interest in including near-field communication (NFC) and wireless power recharging capabilities [5]. This poses the problem of minimizing interference among them [6] to safely ensure the simultaneous communication and recharging operations. Besides the standard solution of dedicated components for each operation (antennas for communication and coil for NFC), it is interesting to investigate the exploitation of the antenna(s) already available in a PDA also for near-field wireless recharging or NFC. The use of reactive fields [7, 8, 9] allows reducing electromagnetic interference and adds security to communication. However, the use of the antennas reactive fields (near-fields) requires complying with a number of challenges, if they should be simultaneously suitable for far-field and near-field operations [10]. In [11], wireless power transmission (WPT) by antennas coupled in the near-field is studied, and the power-transmission efficiency accounts for antenna dimensions and ohmic losses. In [12], a 2.45 GHz monopole is considered for realizing near-field WPT to obtain high transfer efficiency, but the antenna is located in a dedicated docking support and no simultaneous near- and far-field activities are demon-

strated. In my thesis, I start from the preliminary studies provided in [13] and [14] to demonstrate and validate the feasibility of simultaneous near-field and far-field exploitation of the same antenna in a PDA, without resorting to dedicated antenna design and to additional bulky components [15].

I first start with a simple case as a proof of concept where a simple $\lambda/2$ printed dipole has been used. This antenna has been designed for communication purposes at 868 MHz and, when faced with an identical dipole, it is able to wirelessly transfer the power through capacitive coupling at 13.56 MHz. Capacitive coupling between two identical faced antennas has been investigated for simultaneous WPT at 13.56 MHz and communication at 868 MHz.

A deeper investigation has been also carried out. In this case I adopt a rigorous network model of two-faced antennas, accounting for losses, to design a near-field WPT system [9], and to derive a proper embedded network that maximizes the power transfer efficiency, while preserving the data communication. Two dual-band monopoles antennas, geometrically similar to those of modern mobile-phones, are designed for the UHF communication bands (900 / 1800 MHz) and are employed at 433 MHz for bi-directional device recharging. At each antenna port, a three-port lumped-element feeding-network is designed as a suitable frequency diplexer, enabling near-field power transfer and far-field data communication in a seamless way. For each distance under test, a circuit model is extracted whose parameters are derived by full-wave simulation of the entire link [14]. In this way a simple model of the near-field coupling mechanism is available which can be used to predict the rest of the link embedded network topology [9], including losses. Extensive measurements of the realized prototype show that far-field communication and

near-field WPT operations can be simultaneous. A one-way recharging is considered and demonstrated, but the dual power flow in the reverse direction can be taken for granted by symmetry. Since the primary purpose of the system is not WPT but communication, the obtained near-field transfer efficiencies are not as high as in dedicated systems, but they are still significant, considering that wireless recharging of PDAs is enabled by simply adding a simple frequency diplexer to the existing antenna system, without further crowding the wireless device.

Chapter 1

Wireless Power Transfer

Wireless Power Transfer (WPT) can be introduced as the way to transmit electrical energy without wires. Wireless transmission is useful to power electrical devices where interconnecting wires are inconvenient, hazardous, or not possible. There are many different technologies for transmitting energy thorough electromagnetic fields [16, 17, 18, 19].

In general, they differ in the distance over which they can efficiently transfer the power and in the mechanism that can exploit either Far-Field RF sources (FF-WPT) or Near-Field closely located sources (NF-WPT) [20]. Apart distance from the source, another relevant difference between NF- and FF-WPT is the operative frequency range. The FF-WPT employs high frequencies in the range of microwave [21] or millimeter-wave [22] while, on the other side, the NF-WPT employs sources at Low-Frequencies [23] or High-Frequencies [24] ranges.

Clearly, a big difference between radio- and power-communication is the purposes for which they are created. From radio communication side, the goal is the transmission of information and, for this reason, the amount of power that reaches the receiver is not extremely important. Due to this, it is sufficient that the information is only clearly received

[17, 18, 25]. Indeed, in wireless communication technologies it is sufficient that very small amounts of power reaches the receiver. Vice-versa, from the wireless power transmission point of view, the amount of received energy is the primary goal and, for this reason, parameters such us the total received power or the efficiency (ratio between transmitted power on received power) are important [18]. For this reason, wireless power transfer technologies are more limited by distance than wireless communication technologies.

1.1 Field Zones

In general, it is possible to consider an antenna as the way to convert the guided electromagnetic field inside a waveguide, microstrip or transmission line into waves radiated in the free space or vice-versa [26]. A standard communication link consists of two distinct antennas, one operating as a transmitter (TX) and the second one as a receiver (RX). The distance between the TX and the RX antenna, with respect to the operating frequency and the largest dimension of the antenna, defines the operating regions of the antenna. Even if the boundaries between this regions are vaguely defined, it is possible to separate the whole space in two main regions called Far-field (FF) and Near-field (NF). These regions are useful to identify the field structure and to know which simplification can be applied but, as previously anticipated, there is no precise boundary and also no abrupt change in the field configuration.

The FF region (also called Fraunhofer zone) surrounds the inner NF up to an imaginary infinity distance and represents the vast majority of the space where the wave usually travels and this region is the radiating region. Here, the angular field distribution is essentially independent from antenna distance and can be approximated with spherical wave-

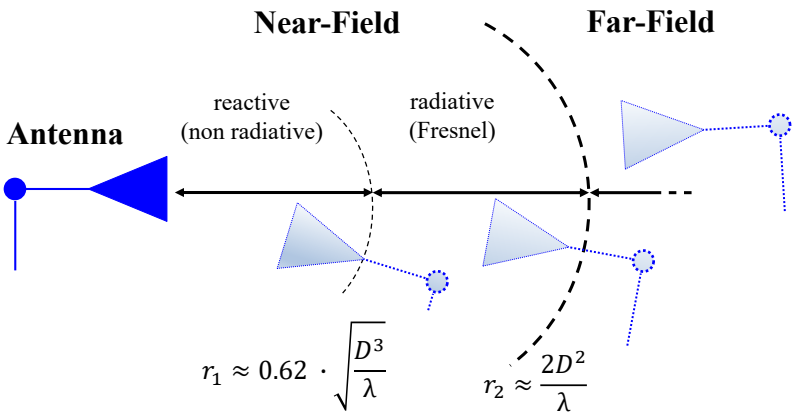

Figure 1.1: Near-Field and Far-Field regions.

fronts. Since we are far from the antenna, its size and shape are not anymore important and we can approximate it as a point source. The electric and magnetic fields are in phase, perpendicular to each other and perpendicular also to the direction of propagation. This greatly simplifies the mathematics and allows to make use of simplified but accurate filed expressions.

On the other side, the NF region can usually be seen as a composition of two sub-regions. The former is called Reactive near-field region. It's a region immediately surrounding the antenna where the reactive field predominates. The electric and magnetic fields are not necessarily in phase to each other and the angular field distribution is highly dependent upon the distance from the antenna and the link direction. Here, only numerical methods (or complex calculations) can determine the actual reactive nature of the field. This region can be considered as a volume that the antenna needs to "arrange" the field that will actually radiate. The latter is called Radiating near-field (or Fresnel) region. It is a region surrounding the previous Reactive near-field region and enveloped by the Fraunhofer region just described above. Here, the radiation field predominates, the electric and magnetic fields are in phase, but the

angular field distribution is still dependent upon the distance from the antenna. This means that, since we are still close to the antenna, the contribution of the different parts of the antenna make the field structure be complex. In other words, we are still too close to the antenna to ignore its shape. Even if the field structure is simpler, it still requires numerical methods (or complex calculations) to determine the exact structure.

As anticipated, the boundaries between these regions are not univocally defined. A possible criterion is the one proposed in [27]. Referring to [27], the first boundary between the Reactive and Radiative near-field regions ca be expressed by:

$$r_1 \approx 0.62 \cdot \sqrt{\frac{D^3}{\lambda}} \tag{1.1}$$

where D is the maximum dimension of the antenna and λ is the wavelength. In general, to be valid, D must also be large compared to the wavelength ($D > \lambda$) [27].

The boundary between the Near-Field and Far-Field regions can be approximately expressed by:

$$r_2 \approx \frac{2D^2}{\lambda} \tag{1.2}$$

Obviously λ can be calculated by $\lambda = \frac{c_0}{f\sqrt{\varepsilon_r}}$ where f is the frequency, c_0 is the speed of light ($c_0 = 299'792'458\ {}^{m}/_{s}$) and ε_r is the relative permittivity of the medium where the antenna is propagating (i.e. $\varepsilon_{r_{air}} \approx \varepsilon_{r_{vacuum}} = 1$).

An overall representation of the boundaries and regions explained above is shown in Fig. 1.1.

The amplitude pattern of an antenna, as the observation distance is varied from the reactive near field to the far field, changes in shape

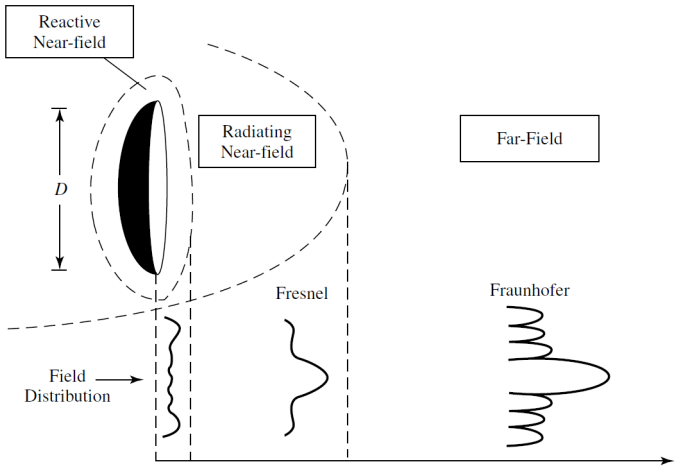

Figure 1.2: Typical changes of antenna amplitude pattern shape from reactive near field toward the far field. [1]

because of variations of the fields, both in magnitude and phase. A typical progression of the shape of an antenna field pattern, with the largest dimension D, is shown in Figure 1.2. It is evident that in the reactive near field region the pattern is more spread out and nearly uniform, with slight variations. As the observation is moved to the radiating near-field region (Fresnel), the pattern begins to smooth and form lobes. In the far-field region (Fraunhofer), the pattern is well formed, usually consisting of few minor lobes and one, or more, major lobes.

1.1.1 Non Radiative Techniques

Before the electrical-wire grid was available, efforts and interest were dedicated (in particular by Nikola Tesla [28]) to develop schemes and techniques to transport energy over short and long distances without any carrier medium (i.e. wirelessly). Problems in this context have been partially solved. Indeed, radiative patterns of omnidirectional antennas (optimally working with information transfer) are not satisfactory for such a goal since the majority of its energy is dissipated into free space. On the other side, using directive radiation patterns (i.e. lasers

or high-directional antennas) can be efficiently used for energy transfer, even for long distances but under the restriction of a continuous line-of-sight and a complex tracking system in the case of mobile objects. However, a more efficient way to wirelessly transfer the power is to rely on non-radiative fields: in this case, the covered distance is sensibly lower, but the overall link efficiency is sensibly higher. The rapid development of autonomous personal digital assistant (PDA) in recent years (i.e. laptops, tablets, mobile phones, house-hold robots, that rely typically on chemical energy storage) justifies investigation of reactive WPT solutions for energy-aware PDAs, thus saving a huge amount of batteries.In general, it is known that non-radiative coupling exploits either electric or magnetic fields. The electric (or capacitive) coupling is characterized by its sensitivity to distance variations and by its high interactivity with the surrounding environment, whereas, for the magnetic (or inductive) coupling is characterized by its low interaction with the surrounding environment and its safety for humans. In both cases, link distances are usually really small (1.2) and this can represent a limit in many applications. In addition to them, efficient mid-range WPT links are also available. They are obtained by using resonant schemes based on magnetic coupling thus resulting in a so called wireless resonant energy link [29, 30, 31]. With respect to non-resonant coupling, resonant techniques allow to extend the link range [32, 33, 34, 35]. At the turn of the 20th century, Nikola Tesla did the first experiments with both resonant inductive and capacitive coupling. In this thesis the Capacitive coupling is exploited and intensively used, even if from a parasitic point of view, i.e. without the use of a dedicated architecture. For this reason, a deeper explanation of this specific coupling is required.

1.1.2 Capacitive coupling

In the capacitive coupling (CC), energy is transferred by electric fields [18] between a couple of electrodes (i.e. metal plates). When the transmitter electrode faces the receiver one they form a capacitor where the medium in between plays the role of the capacitor dielectric [18, 25, 36, 19, 37]. An oscillating voltage generated by the transmitter is applied to the transmitting plate, thus inducing an oscillating potential on the receiver plate. This is due to a transmitting oscillating electric field that, by electrostatic induction [18, 37], induced an oscillating current into the load circuit. The total power transferred between the two faced plates increases with the frequency, the square of the voltage across the parallel plates and the capacitance between the plates [37]. Regarding the capacitance value, it is plain to understand that it is proportional to the smallest plate area and inversely proportional to the distance that separates the two plates [18].

Capacitive coupling has only been used practically in a few low power applications, because of the very high voltages on the electrodes required to transmit significant power that can be unsafe [25, 36] and, additionally, because it can be source of undesired side effects like noxious ozone production [38]. In addition, in contrast to magnetic fields [39], electric fields strongly interact with most of the existing materials, including the human body, due to dielectric polarization [40]. Materials placed in between, or even nearby, the electrodes can absorb the transmitted energy and, in the case of humans, determine an excessive unhealthy electromagnetic field exposure [25]. However, despite all the aforementioned disadvantages, capacitive coupling has also a few advantages with respect to the inductive coupling. Firstly, in capacitive coupling the field is predominantly confined between the capacitor plates, thus reducing

the interference that, in inductive coupling, can be avoided only through a large employment of ferrite "flux confinement" cores [18, 40]. In addition, alignment requirements between the transmitting and receiving plates are less critical than for coil link [18, 25, 37]. Mainly this aspects has increased the interest in capacitive coupling, by inspiring the application to charge portable devices battery [41] and it is also being considered as a mean for transferring power between different substrates in multi-layer integrated circuits [42]. For these purposes, two types of architecture deploying capacitive coupling can be resumed:

- **Bipolar** design [43, 44]: In this type of circuit, there are two transmitting plates and two receiving plates. Each transmitter plate is coupled to a single receiver plate. The transmitter oscillator drives the two transmitter plates in opposite phase (180° phase difference) by a high alternating voltage, and the load is connected between the two receiver plates. The alternating electric fields induces opposite phase alternating potentials in the receiver plates, and this "push-pull" action causes current to flow back and forth between the plates through the load. A disadvantage of this configuration for wireless charging is that the two plates in the receiving device must be aligned face to face with the charger plates for the device to work [19].

- **Unipolar** design [18, 37, 44]: In this type of circuit, the transmitter and receiver have only one active electrode, and either the ground or a large passive electrode serves as the return path for the current. The transmitting oscillator, as well as the load, are connected between an active and a passive electrode. The electric field produced by the transmitter induces an alternating charge

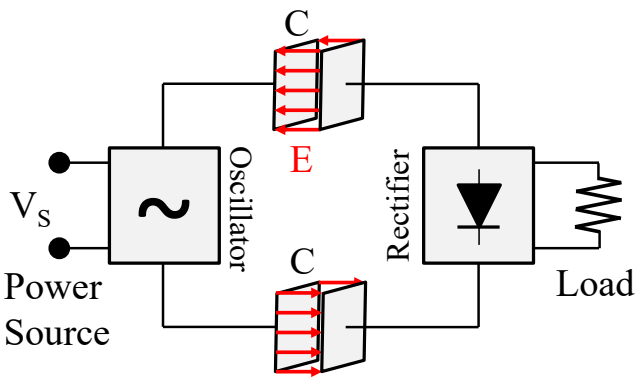

Figure 1.3: Bipolar coupling system for Capacitive WPT.

displacement current in the receiving plate through electrostatic induction [45].

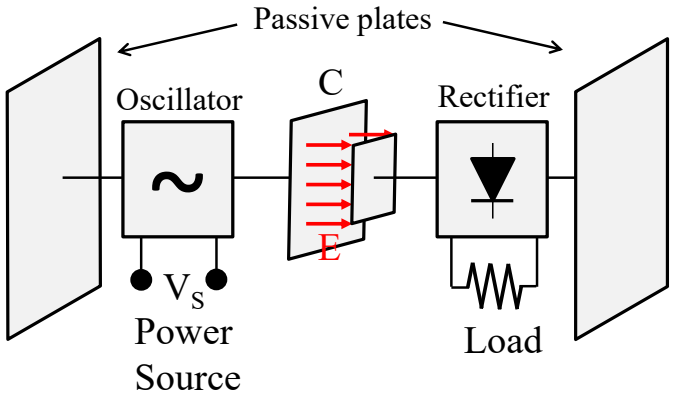

Figure 1.4: Unipolar coupling system for Capacitive WPT.

1.2 System performance maximization

With reference to Fig. 1.5, and with respect to the aforementioned and more common unipolar architecture, it is possible to consider the general two-port representation of the communication link between two coils/plates/antennas, which can be either placed in their near- or far-field zones [46]. It consists of a reciprocal two–port lossy network (i.e.

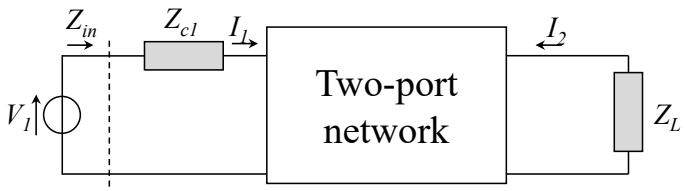

Figure 1.5: Two–port network with added matching impedance $Z_{c1} = R_{c1} + j \cdot X_{c1}$ and load impedance $Z_L = R_L + j \cdot X_L$. The relevant parametrization is provided in Table 1.1.

$z_{12} = z_{21}$), represented by its impedance matrix, with elements $z_{ij} = r_{ij} + j \cdot x_{ij}$, with $i, j = 1, 2$, that can be described as follows:

$$\begin{cases} v_1 = z_{11} i_1 + z_{12} i_2 \\ v_2 = z_{12} i_1 + z_{22} i_2 \end{cases} \tag{1.3}$$

The elements of the impedance matrix can be obtained either by simulation or by measurement. We will denote by P_{in} the active input power delivered from the generator to the two port network and by P_L the active power delivered to the load impedance Z_L. We can thus define the link efficiency as $\eta = P_L/P_{in}$. This choice is similar to that used in [47, 48]. For this case we address the problem, with reference to Fig. 1.5, to find suitable values for the load impedance $Z_L = R_L + j \cdot X_L$, and for the matching impedance Z_{c1} in order to establish a reliable link between the two coils/plates/antennas. It has been shown that two possible approaches are feasible:

- maximize the efficiency (defined as the ratio between the active power delivered to the load -i.e. R_L- with respect to the active power provided by the generator);
- maximize the power delivered to the load.

In particular, depending on the selected approach, different values for Z_L, Z_{c1} are required and different results for efficiency and power hand-

Table 1.1: Analytical computation of the parameters of Fig. 1.5 for different design specifications on Maximum Power and on Maximum Efficiency ($\chi = x_{12}/\sqrt{r_{12}r_{22}}$, $\xi = \sqrt{r_{11}r_{22}}$, $\theta = \sqrt{1+\chi^2}\sqrt{1-\xi^2}$, $\theta_x = \chi\xi$, powers are normalized to $P_0 = V_1^2/2$).

Parameter	*Maximum efficiency*	*Maximum power*
R_L	$r_{22}\theta_r$	$r_{22}\theta_r/\left(\theta_x^2+1\right)$
X_L	$r_{22}\theta_x - x_{22}$	$r_{22}\theta_x - x_{22} + \frac{r_{22}\theta_x\theta_r^2}{\theta_x^2+1}$
R_{c1}	0	0
X_{c1}	$x_{12}r_{12}/r_{22} - x_{11}$	$x_{12}r_{12}/r_{22} - x_{11}$
R_{in}	$r_{11}\theta_r$	$r_{11}\theta_r^2/\left(1+\theta_r^2+\theta_x^2\right)$
X_{in}	0	0
P_{in}	$\frac{1}{\theta_r r_{11}}$	$\frac{1+\theta_r^2+\theta_x^2}{2\theta_r^2 r_{11}}$
P_L	$\frac{\eta_1}{\theta_r r_{11}}$	$\frac{\xi^2+\chi^2}{4\theta_r^2 r_{11}}$
η	$\eta_1 = \frac{\xi^2+\chi^2}{(1+\theta_r)^2+\theta_x^2}$	$\frac{\xi^2+\chi^2}{2(1+\theta_r^2+\theta_x^2)}$

ling are achieved. In Table 1.1 we have summarized the parametrization for the different choices. Therefore, at a single frequency point, we may select one approach, i.e. maximize efficiency and save power, or the other one to obtain maximum power on the receiving antenna.

Results in terms of Z_L, X_{c1} can significantly change depending on the selected approach. As an example, it is possible to check the values listed in Table 2.1 where the initial proof of concept of this work has been investigated carried our exploiting two simple printed dipoles faced at $2\,mm$, $5\,mm$ and $10\,mm$ distance. Further details are given in the following Chapter.

Chapter 2

Proof of Concept

For the proof of concept here investigated, it is necessary to recall that the goal of this work is to investigate the possibility to exploit antennas designed for communication purposes, and already available in PDA, for WPT too. The goal is, also, to allow and realize a simultaneous wireless information and power transfer (SWIPT).

As a first step, I decided to investigate if, exploiting two simple printed dipoles, it is possible to establish a capacitive link sufficiently efficient. For this reason, a $\lambda/2$ printed dipole has been selected and designed to operate for communication purposes at 868 MHz. Its layout is shown in Fig. 2.1.

The standalone antenna input reflection coefficient and E- / H-plane radiation patterns at 868 MHz, as computed from a full–wave simulator (CST Microwave Studio [49]), are shown by red lines in Fig. 2.4 and 2.5, respectively.

For this proof of concept, two identical dipoles are then faced at several distances, namely 2, 5 and 10 mm, and the behaviour of the obtained two-port reactive network is investigated at 13.56 MHz. Indeed, referring to (1.1), at this operating frequency the two dipoles are

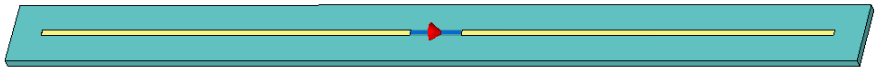

Figure 2.1: Half-wavelength printed dipole resonanting at 868 MHz.

in the near-field region of each other, their radiation properties are negligible and almost only reactive fields are involved. In the present case, a capacitive coupled WPT link is established and investigated.

2.1 Decoupling network

In order to allow the coexistence of the two different antenna operations, the balanced decoupling network plays a strategic role. Connected to the antenna port, this important block has been investigated and designed in this section. A circuit schematic of a possible topology is shown in Fig. 2.2. This solution allows the WPT at 13.56 MHz and the communication at 868 MHz, of course these operations by the same antenna have to be completely decoupled, in order to allow the simultaneous wireless information and power transfer (SWIPT) activities. Indeed, when port 2 is excited at 868 MHz, port 1 is decoupled by the choke inductance L_1, which also acts as the resonating component of the capacitive link. In this condition the signal can be totally radiated by the dipole.

Similarly, when power is transmitted at 13.56 MHz through port 1, port 2 is decoupled by the parallel resonance (L_R and C_R) at the same frequency. At 868 MHz, this result is demonstrated by the plots of Figs. 2.4 and 2.5 where the antenna input reflection coefficient and far-field performance, computed by electromagnetic simulation, are plotted for several dipoles distances. Indeed, the proximity of another antenna degrades the far-field properties, but without jeopardizing its operating

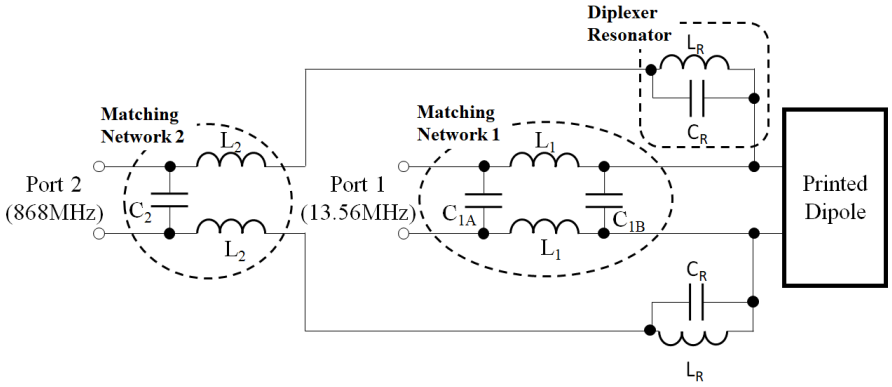

Figure 2.2: Circuit topology of the feeding network of the two-operation antenna.

conditions.

The block schematic of a possible final link configuration is shown in Fig. 2.3, under the not restricting assumption that two identical devices are used for power transfer.

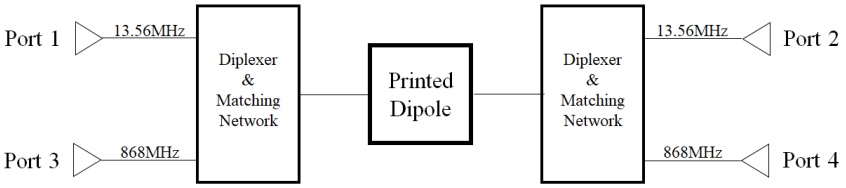

Figure 2.3: Block schematic of the final link configuration for simultaneous exploitation of an antennas pair for near-field WPT and far-field communication.

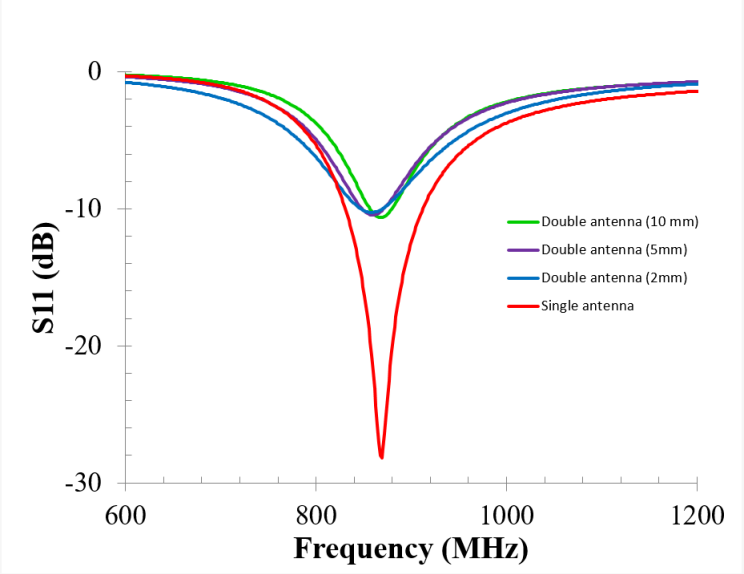

Figure 2.4: Input reflection coefficient of the half wavelength dipole antenna, stand alone and with an identical dipole faced at different distances.

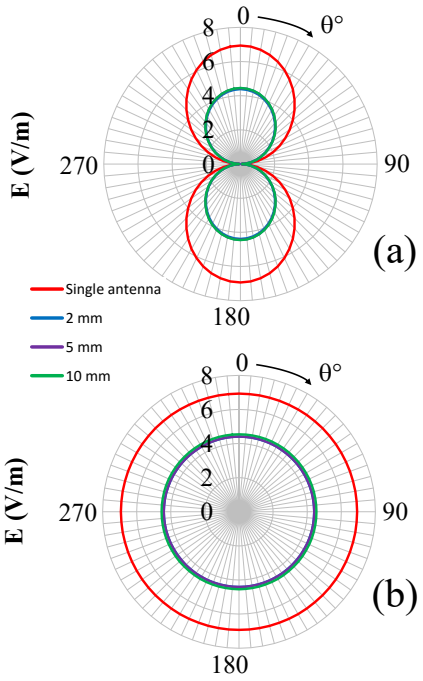

Figure 2.5: E-plane (a) and H-plane (b) radiation pattern of the standalone halfwavelength dipole (red line) and in the presence of an identical one, faced at 2, 5 and 10 mm.

2.2 Performance maximization

At each operating frequency, the input and output optimal impedances can be finally computed, either for maximum efficiency or for maximum power transfer, by following the rules summarized in Table 1.1. At 13.56 MHz, the network parameters, computed for several dipole distances, are listed in Table 2.1.

For each link distance these analytical results are then used in realistic operating conditions, that is including losses for both the inductors and the capacitors. In addition, this work is thought for storing energy in a chosen device (or PDA) and not for supplying power to it. For this reason, it is important to minimize the energy loss along its entire path in order to store as much as possible energy inside the chosen device (or PDA). By means of circuit simulations based on Harmonic Balance technique [50, 51], a final design of the four ports network of Fig. 2.3 is carried out with specification on maximum efficiency: in this step, a unique circuit topology is adopted for various dipole distances and the best trade-off is searched. The results are summarized in Fig. 2.6 and Fig. 2.7 and the corresponding circuit parameter values are listed in Table 2.2. In Fig. 2.6a the input reflection coefficient at port 1 of Fig. 2.3 is plotted versus frequency with the dipoles distance as the parameter. A good matching is obtained for the different distances, apart from the closest one, which can be explained by the over-coupling phenomenon [52]. In Fig. 2.6b the transmission coefficient between the communication and the power transfer ports proves the feasibility of the coexistence of the two operations. In Fig. 2.7 the efficiency prediction is plotted when adopting a unique circuit for the considered distances (dashed line). Comparisons with the results obtainable by optimizing dedicated networks for each distance are also superimposed in the same

Table 2.1: Matching Network element values for different dipoles distances. A 1V source has been used (powers are normalized to $P_0 = V_1^2/2$).

	2mm		*5mm*		*10mm*	
Parameter	η_{MAX}	P_{MAX}	η_{MAX}	P_{MAX}	η_{MAX}	P_{MAX}
R_L (Ω)	9754.8	460.20	8090.1	12.38.0	5628.5	3492.20
X_L $(k\Omega)$	12.92	-4.84	15.80	-8.32	17.57	-11.16
R_{c1} (Ω)	0	0	0	0	0	0
X_{c1} $(k\Omega)$	13.01	1.31	16.05	18.84	17.60	17.60
R_{in} (Ω)	9624.9	210.4	7501.3	231.7	5594.9	253.1
X_{in} (Ω)	0	0	0	0	0	0
P_{in} (mW)	0.104	4.24	0.133	4.32	0.179	3.95
P_L (mW)	0.102	2.37	0.129	2.16	0.171	1.97
η (%)	97.8	50	97	50	95.6	50

Table 2.2: Final Values of the components of Fig. 2.2.

Parameter	*Value*
L_1 (μH)	22.8
L_2 (nH)	13.45
L_R (μH)	46
C_{1A} (pF)	388.6
C_{1B} (pF)	15.08
C_2 (pF)	26.71
C_R (pF)	3

plot (solid line). In addition, it is important to spend a couple of words on the values of efficiencies obtained. Indeed, comparing the results predicted in Table 2.1 with respect to the ones plotted in Fig. 2.7 for a dedicated network for each distance considered, we can see a reduction of the nominal values of the efficiencies. This is due to the selected commercial lumped elements, and their low Q-factor, adopted for Fig. 2.7 with respect to the ideal ones used for the estimation of efficiencies listed in Table 2.1.

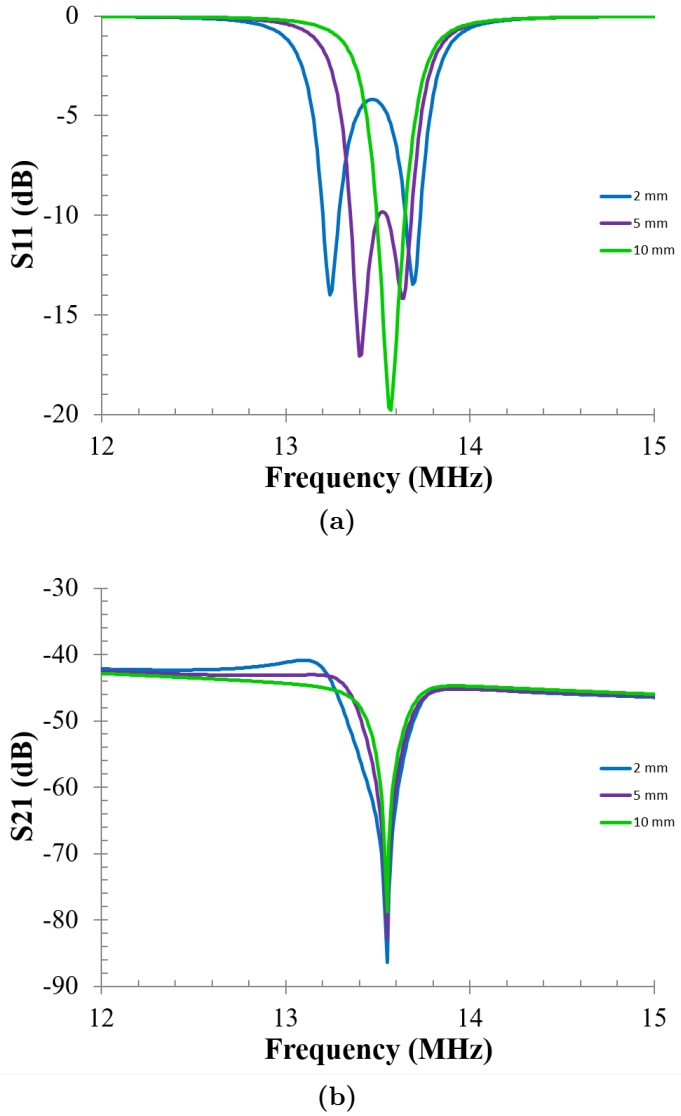

Figure 2.6: Reflection (a) and transmission (b) coefficients behaviour of the final link of Fig. 2.3 in the frequency band around 13.56 MHz.

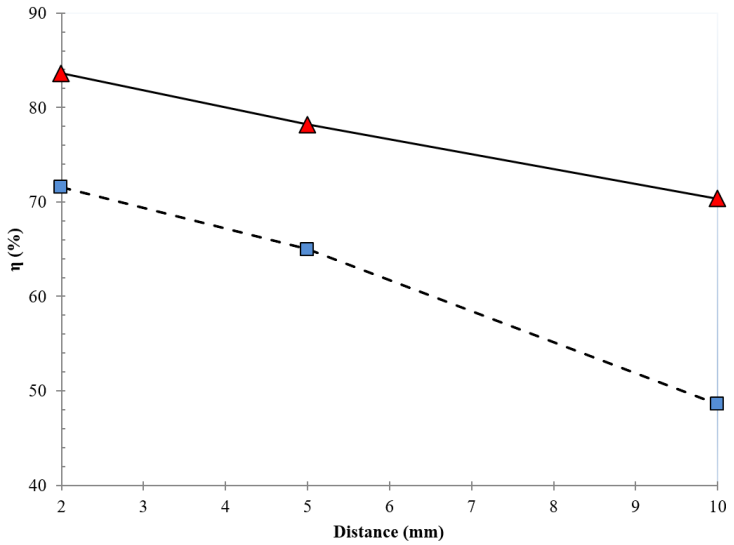

Figure 2.7: Predicted link efficiency with a unique circuit (dotted line) and with a dedicated network for each distance (solid line).

2.3 Practicability of the proposed idea

With this proof of concept, the possibility to use antennas, typically operating for communication purposes, for wireless power transfer, too, has been demonstrated [53]. It has been shown that, by properly selecting the matching networks at the frequency of interest, it is feasible to design a simple system that allows to use the same antenna for both communication and wireless power transfer. Therefore it has been shown that, by using the simple network reported in Fig. 2.2 and Fig. 2.3, we can exploit the dipole behaviour in the communication band at 868 MHz, while achieving wireless power transfer capabilities at the frequency of 13.56 MHz.

Chapter 3

Practical demonstration of SWIPT capability

In this Chapter, I exploit the previously introduced concepts and the proof of concept. In particular, it is worth noting the new choice of a higher wireless power transfer frequency. Indeed, when trying to implement and realize the lumped element circuit at 13.56 MHz not practical element values were obtained. This was due to the really weak coupling created between the antennas and to the low WPT frequency fixed, thus leading to too big nominal values of the lumped elements and, for the inductors required for the resonance network, to high losses. For this reason, and because of the impossibility to increase the capacitive coupling between very thin antennas, the choice has been to increase the frequency for the wireless power transfer by adapting the ISM 433 MHz band and, consequently, in order to reduce the radiation at f_{WPT} (I want the antenna to not radiate at f_{WPT} and be seen as a pure reactive load), also the communication frequency has been raised ($f_{WPT} < f_{COMM}$).

3.1 Antenna feeding network for simultaneous operations

As anticipated, current PDAs and cell phones are overcrowded by several antennas to cover the GSM (900 MHz and 1800 MHz), UMTS (2150 MHz) and WiFi (2450 MHz) bands. If these antennas are also properly exploited at lower frequencies, a concurrent near-field link among different mobile devices can be realized, for re-charging or NFC purposes, without significantly affecting their far-field communication activities. This can be achieved by equipping the antennas with suitable feeding networks, to guarantee the co-existence of such different wireless operations (at the related operating frequencies). By facing a pair of such PDAs equipped with this network, a near-field WPT link can be established. A schematic block diagram of one half of the proposed solution is shown in Fig. 3.1: it represents a mobile handset, which can be placed in close proximity to another one, to enable a reactive near-field coupling for WPT, while preserving the far-field communication capabilities of each other. The chosen antenna layout, which is detailed in section 3.2, is also shown in Fig. 3.1, together with its geometrical dimensions. A dual-band dipole antenna, covering the GSM900 and GSM1800 bands for communication and exploiting the ISM 433 MHz band for WPT purposes, has been chosen. A ground plane with dimension similar to typical cell phones has been considered to emulate the real application: it is worth noting that the ground plane size results to have almost no effect on both the communication and the power transmission behaviour. The frequency separation, between far- and near-field antenna operations, allows a reliable design of a frequency-division antenna feeding network. This consists of a three-port diplexer, with high isolation between the WPT and communication ports and high trans-

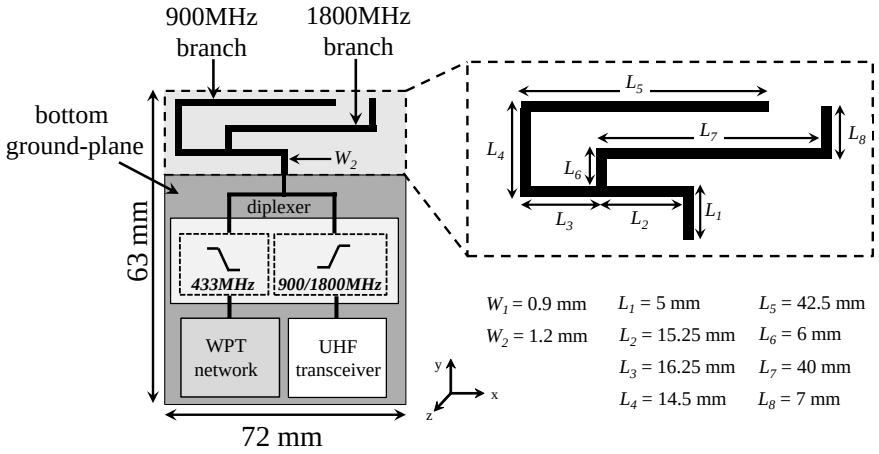

Figure 3.1: Schematic block diagram of the PDAs sub-system with the antenna for simultaneous far-field communication and near-field power transfer, and the corresponding printed antenna layout.

mission between both WPT and communication ports with the matched antenna port. The lumped-element equivalent circuit of the reactively coupled handsets is shown in Fig. 3.2: the main coupling mechanism is capacitive and is represented by C_{link}, which varies with link distance, while the two series-connected RLC branches (R_{Bi}, L_{Bi}, $i = 1, 2$ and C_f), at each side of the link, models the metallization losses, inductive and fringing effects, respectively, whereas k_1 and k_2 account for the consequent parasitic inductive coupling (weak). For any other couple of faced-antennas a suitable equivalent circuit can be derived as well.

3.2 Dual-band printed antenna and far-field performance

Printed antennas solutions are preferred for their light-weight, compact size, ease of manufacturing, and ease of integration with the associated

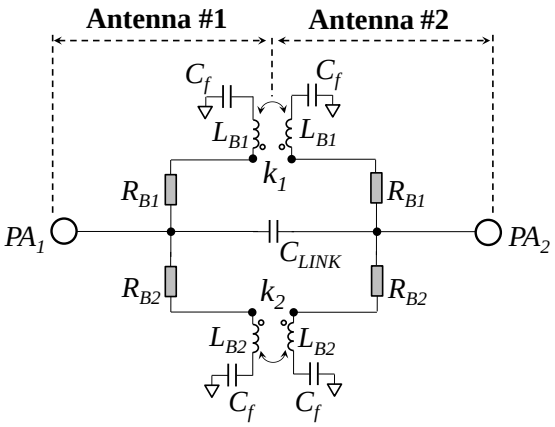

Figure 3.2: Equivalent circuit model of the capacitive link realized by two faced antennas at the WPT frequency.

circuitry. Several topologies have been proposed to be compatible with the handsets shells, as multiband monopoles [54], PIFA [55] and 3D antennas [56]. The dual-band printed dipole layout similar to the one in [57] has been selected and is shown in Fig. 3.1: it consists of a planar two-branch wire antenna, whose arms share the same 50Ω microstrip feeding line, and are printed on the ungrounded portion (light-grey in the figure) of a Taconic substrate RF-60A ($\varepsilon_r = 6.15$, $tan(\delta) = 0.0028$, $thickness = 0.635mm$). Maximization of the radiation efficiency and minimization of port mismatch are simultaneously achieved by properly varying the design parameters, i.e. the strips length reported in Fig. 3.1. Low-directive behaviour at both operating frequencies is searched during the design process, thus enabling antenna transmission/reception capability in a wide range of directions. No additional antenna optimization has been carried out for near-field operation at 433 MHz. Fig. 3.1 shows the final layout dimensions. Note that the chosen antenna topology is only one choice among a wide range of possibilities: this work aims to demonstrate the feasibility of the WPT operation exploiting strip-like antennas available in modern PDAs. Full–wave simulation

[49] of the standalone antenna in terms of input reflection coefficient and normalized radiation patterns are given in Figs. 3.3 and 3.4 by solid lines, whereas dashed lines represent measurements. Good agreement is observed in Fig. 3.3, with a reflection coefficient lower than $-15dB$ in the two bands: the slight frequency shift (100 MHz) in the upper band is probably due to mechanical tolerances in the prototype realization on the adopted thin and soft substrate. The comparison in terms of normalized E-field radiation patterns in the H- and E- planes is very satisfactory as well. From inspection of Fig. 3.4, the antenna radiation mechanism is easily retrieved: at 900 MHz the radiation pattern is almost omnidirectional in the H-plane (XZ-plane), as expected from the y-aligned monopole behaviour of the left antenna branch; a bit more directive pattern occurs at 1800 MHz because of the contribution of two x-aligned dipoles in a Yagi-Uda-like configuration. This is confirmed by Fig. 3.5, where the simulated surface currents are reported: the monopole-like behaviour at 900 MHz (Fig. 3.5a), with the ground acting as an electric symmetry plane, is demonstrated by the zero current value at one edge, only, of the left branch; conversely, at 1800 MHz (Fig. 3.5b), the two involved arms are horizontal dipoles with almost zero current at both ends and maximum current in the centre of the arms. The surface current plots at the WPT frequency of Fig.3.5c show a weaker (and almost static) behaviour and the antenna arms act as thin metallic plates: this confirms the needed behaviour of the antenna at 433 MHz as a non-radiating element.

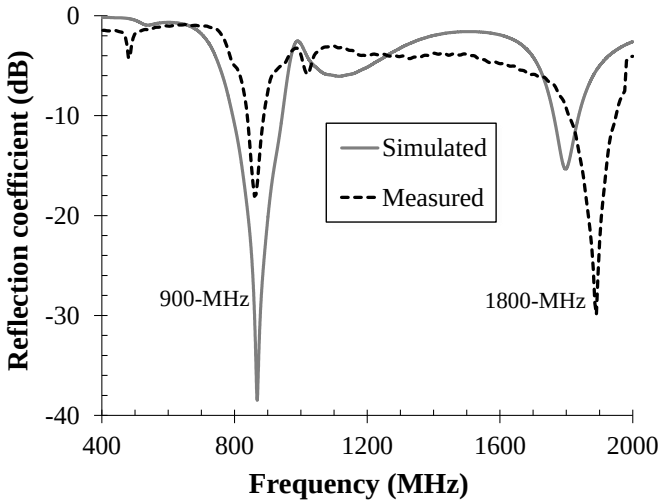

Figure 3.3: Simulated and measured reflection coefficient of the dual-band dipole antenna of Fig. 3.1.

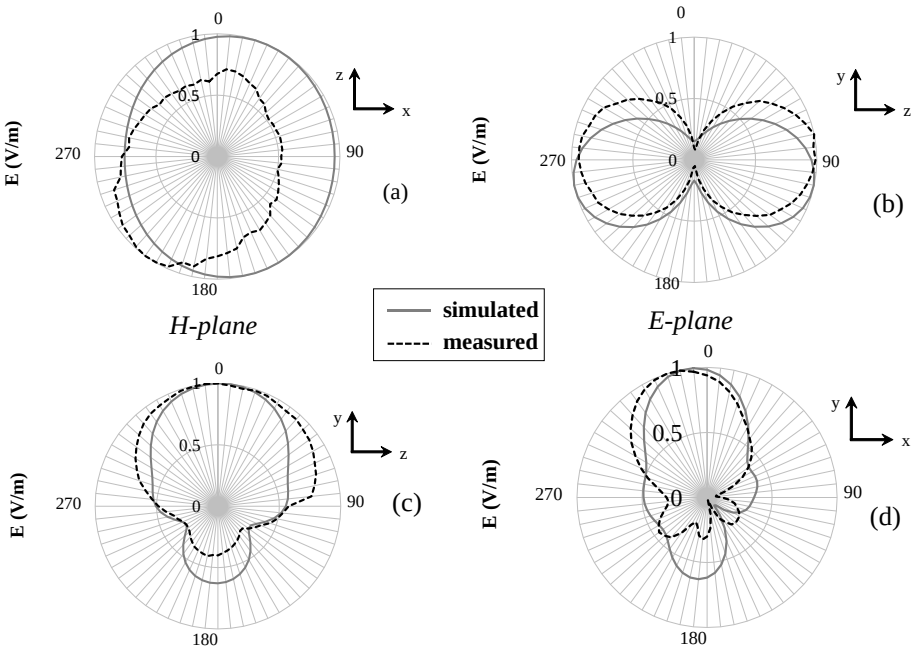

Figure 3.4: Simulated and measured normalized E-field radiation patterns in H-plane and E-plane of the standalone printed antenna at 900 MHz ((a) and (b)) and 1800 MHz ((c) and (d)) (linear scale).

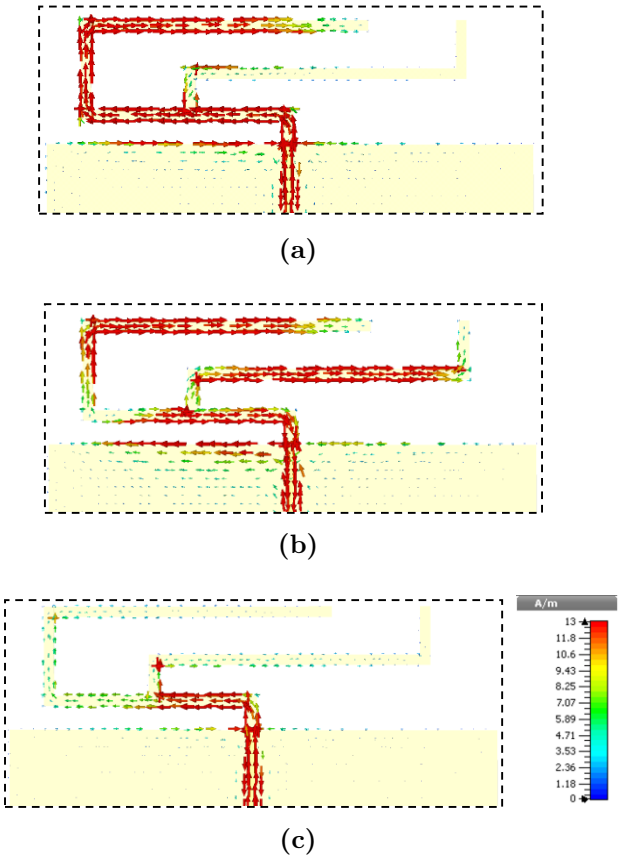

Figure 3.5: Simulated surface current distribution of the antenna at: (a) 900 MHz, (b) 1800 MHz and (c) 433 MHz (not resonant).

3.3 The printed antennas faced for near-field WPT

If two similar antennas are located in close proximity, a power transfer capacitive link is obtained by exploiting the near-field weak coupling between the thin metallizations. This dual configuration with respect to a magnetically (or inductively) coupled link [5, 8] can be explained by the circuit model of Fig. 3.2 whose parameters can be derived from the full-wave simulation of the two faced antennas, for any distance between them. Three reference distances (D) are considered, namely 10, 20 and 30 mm, to cover different mobile phones cases (for the slimmest ones a 15-mm distance is realistic). The usefulness of the circuit model is manifold: i) it gives a simple representation of the capacitive coupling mechanism between the two-faced antennas; ii) it allows a fast prediction of the frequency behaviour of the WPT link; iii) it provides a straightforward estimate of the components to be embedded at each antenna side for a resonant capacitive link [9]. Indeed the obtainable coupling is weak and the resonance condition is mandatory to enhance the link transfer efficiency. This requires high inductances (L_R) to resonate with the weak capacitive link (modelled by C_{LINK} in Fig. 3.2), according to the well-known relationship:

$$f_0 = \frac{1}{2\pi \cdot \sqrt{L_R \cdot C_{LINK}}} \tag{3.1}$$

However, high inductances imply high losses and thus a drastic drop in the link efficiency itself. Thus 433 MHz ensures lower inductances values with respect to the lower allowed WPT frequencies. But at higher frequencies the antenna could radiate, thus affecting again the link efficiency, and losses increase, too; for these reasons the frequency choice

Table 3.1: Comparison between full-wave and equivalent circuit scattering parameters at 433 MHz, with the circuit parameters of Table 3.2.

D (mm)	*S11*			
	Magnitude (lin)		*Phase (Deg)*	
	EM Sim.	*Model*	*EM Sim.*	*Model*
10	0.92	0.97	-44.50	-44.47
20	0.94	0.99	-39.97	-39.88
30	0.94	0.99	-39.81	-38.80

D (mm)	*S12*			
	Magnitude (lin)		*Phase (Deg)*	
	EM Sim.	*Model*	*EM Sim.*	*Model*
10	0.21	0.23	44.93	45.53
20	0.09	0.10	52.12	50.12
30	0.94	0.99	-39.81	-38.80

Table 3.2: Reactive link equivalent circuit parameters of Fig. 3.2 at 433 MHz and 10, 20, 30 mm antennas distance, with:$L_{B1} = 91nH$, $L_{B2} = 71.2nH$, $R_{B1} = 0.15Ohm$, $R_{B2} = 0.12Ohm$.

D (mm)	$C_{LINK}(pF)$.	$C_f(pF)$	$k_1(10^{-4})$	$k_2(10^{-4})$
10	0.99	0.63	139	8.1
20	0.43	0.66	37	92
30	0.25	0.68	2.4	23

is a delicate trade-off among several opposite needs. 433 MHz is finally adopted since at this frequency the dipoles act as electrically small antennas and their reactive fields, only, are involved, as shown in Fig.3.5c.

For each link distance, the circuit parameters of Fig. 3.2 are optimized with the goal of minimizing the differences between the scattering parameters calculated by full-wave [49] and by circuit [58] simulations of the link. In all cases, a very good agreement is obtained and it is summarized in Table 3.1; this also validates the circuit model itself, to represent the near-field coupling of the faced antennas. The corresponding parameters are given in Table 3.2.

3.4 Design of the diplexer for antenna feeding

Fig. 3.6 shows the circuit model of the link with each antenna port (A_1 and A_2) fed by a three-port diplexer, to simultaneously enable dual-band communication at UHF, through ports 2 and 3, and wireless power transfer at 433 MHz, through ports 1 and 4. The WPT path consists of a one-stage low-pass filter, and the communication path of a two-stage high-pass filter. The WPT branch also includes the proper network to resonate with the weak capacitive coupling to maximize the RF-to-RF power transfer efficiency (η_{LINK}), which is affected not only by the distance-dependent weakly-coupled link, but also by the Q-factor of the resonant networks [9]. When a rectifier is connected to the receiving WPT port, the overall link conversion efficiency can be computed as:

$$\eta_{WPT-LINK} = \eta_{LINK} \cdot \eta_{RF-DC} = \frac{P_{OUT}^{WPT}}{P_{IN}^{WPT}} \cdot \frac{P_{DC}}{P_{OUT}^{WPT}} \tag{3.2}$$

where η_{RF-DC} represents the efficiency of the rectifier, and P_{IN}^{WPT}, P_{OUT}^{WPT} and P_{DC} are the RF powers at the input and output ports of the WPT path (see Fig. 3.6). Thus $\eta_{WPT-LINK}$ depends on both the non-linear behaviour of the RF-to-DC converter and the achieved matching conditions of the resonant link.

The non-linear circuit design of the link of Fig. 3.6 is carried out in two steps: i) for all the considered distances, a unique resonant network is derived to maximize the power transfer efficiency (between ports 1 and 4) and to provide high isolation between the communication and WPT paths; ii) a non-linear optimization, simultaneously carried out at different power levels, defines the proper matching at 433 MHz between the full-wave rectifier and the input WPT port (port 1). Power levels of the order of mW are considered for the present proof-of-concept design,

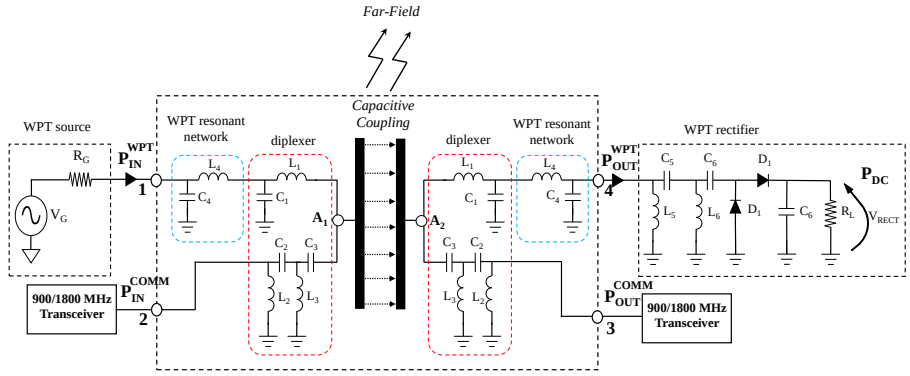

Figure 3.6: Circuit schematic of the entire dual-mode sub-system of two faced PDAs: the three-port diplexers, the components for a resonant capacitive WPT link, and the rectifier network at the receiving side are put into evidence.

in order to be able to validate it in our lab. However, the proposed design procedure can be straightforwardly scaled up to higher power levels by adopting the proper rectifying devices and matching networks. Data- and power- port isolation better than $20\,dB$ and η_{LINK} better than 50, 30%, 15% (at 10, 20 and 30 mm distance, respectively) have been obtained using realistic inductances and capacitances to include losses and parasitic reactive behaviour. A voltage-doubler topology, as in [59], has been chosen for the rectifier, to be matched to the resonant link by the lumped-element π-network of Fig 3.6. Skyworks SMS7630-079 Schottky diodes have been used. The optimization is carried out in a $20dB$ input power range ($-10\,dBm$ to $10\,dBm$) to properly model the power-dependent input impedance of the RF-to-DC converter, focusing on typical near-field WPT scenarios. All the lumped elements of the rectifier, including the load resistance R_L, are used as design variables. It is noteworthy that accurate modelling in the largest possible power range is mandatory since the power-dependent nonlinear rectifier input impedance is the resonant link load and it determines the overall efficiency (3.2). For the same reason, accurate diode package parasitic

models are needed, and those derived in [60] are adopted in the present design. The SMD capacitors are Murata GRM1885 and the inductors are Coilcraft LD0402. The final circuit parameters are listed in Fig. 3.6.

3.5 Misalignment influence on efficiency

Another aspect that has to be taken into account, is the influence of a possible misalignment of the antennas (i.e antennas non perfectly facing each other) on the estimated efficiency. With this goal, the configuration of two antennas faced at 20mm has been considered and the RF-to-RF transfer efficiency is calculated exploiting the simulated four-port scattering parameters (Fig. 3.6) through the equation [61]:

$$\eta_{LINK}(d) = \frac{|S_{41}(d)|^2}{1 - \left|S_{11}(d)^2\right|} \tag{3.3}$$

As just written above, in this section the distance between two faced antennas has been fixed to $20\,mm$ but, to generalize, equation (3.3) is written for a generic distance.

Starting from the perfectly faced antennas investigated before, in CST [49] displacements in both X and Y-axis (refer to Fig. 3.1) within a range of $[-30, +40]$ and $[-20, +20]$ mm, respectively are simulated. Both ranges of X- and Y-range are chosen in order to allow maximum misalignment between the faced antennas. For each configuration simulated in CST, I exported its Touchstone file in order to have a complete electromagnetic characterization of each state necessary for the accurate efficiency calculation. In addition, from ADS [58] I exported the same type of file representing the behaviour of the lossy network used to design the WPT resonant network and the diplexer (Fig. 3.6). In a further step, Matlab [62] has been exploited in order to combine the

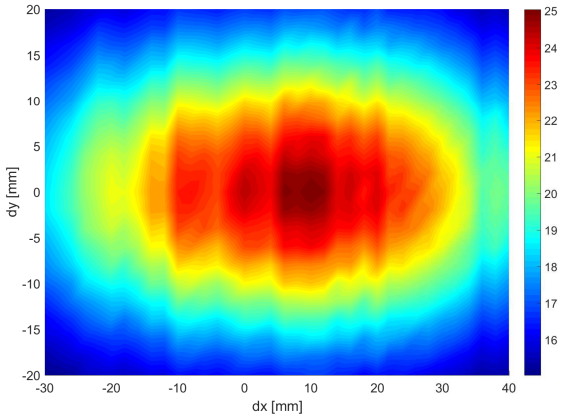

Figure 3.7: Representation of the efficiency when antennas are not perfectly faced ($dx = dy = 0$). dx (respectively dy) represents the displacement along horizontal (respectively vertical) direction in mm. The colour-scale, on the right side of the image, represents the efficiency calculated with (3.3) and expressed in percentage.

touchstone previously created. Indeed, passing through the T parameters (chain scattering or chain transfer) [63], it is possible to easily combine the cascade of different scattering parameters in an unique one [64]. By following [61], the efficiency has been calculated through Eq. (3.3) and then represented in Fig. 3.7 for better understanding.

From Fig. 3.7 is possible to note that antennas maintain high efficiency along the X-axis than along to the Y orientation. This is mainly due to the shape of the antenna itself. Indeed, referring to Fig. 3.1, we can see how the antenna itself covers in the X-direction a length approximatively 2.5 times bigger than in the Y-direction. In addition, when moving in Y-direction, after roughly $20\,mm$ we have the transmitting antenna facing with the shield of the receiving one breaking down any possible coupling.

Furthermore, it is possible to see the maximum coupling in a slightly shifted position ($10\,mm$) with respect to the perfectly faced configura-

tion. Once again, this is probably due to the asymmetric design of the antennas.

Thanks to results plotted in Fig. 3.7, we can see how a misalignment of $40 \times 15\,mm^2$ in the X- and Y-direction respectively has no critical influence on the link efficiency.

Chapter 4

Experimental characterization

4.1 Power transfer measurements

The two sides of the system of Fig. 3.6, including the dual-band printed antennas, have been fabricated on a Taconic RF-60A substrate ($\varepsilon_r = 6.15$, $thickness = 0.635mm$) and the photo of the prototype of one side of the link of Fig. 3.6, with a separated rectifying section, is shown in Fig. 4.1. A testing port has been added to measure the antenna performance in stand-alone configuration.

Representative results of the realized entire four-port network are shown in Figs. 4.2 and 4.3, in terms of scattering parameters. In Fig. 4.2 the measured WPT/communication ports isolation (ports 1-2 or 3-4 of Fig. 3.6) is plotted versus frequency: at the communication frequencies isolation is better than $30dB$, whereas at the WPT frequency band it is better than $20dB$: this is not a concern since the UHF transceiver of any PDAs is always equipped with a high-pass filter [65]. It can be concluded that simultaneous WPT at 433 MHz and communication at

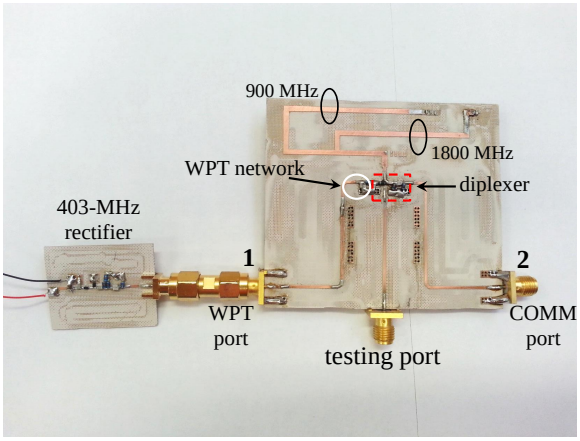

Figure 4.1: Prototype of the dual-band planar antenna system arranged for simultaneous data communication and energy transfer: the lumped-element diplexer, the resonant network and the rectifier are highlighted.

900 and 1800 MHz, with the same antenna, can be accomplished by the proposed system configuration and a communication signal can be safely radiated by the antenna in the presence of the WPT path and vice versa. Figs. 4.3a and 4.3b show the comparison between simulated and measured scattering parameters of the unique two-port WPT network (ports 1-4) for variable distances between the antennas: a good trade-off is obtained by the designed topology, the worst case being the 30-mm distance (S41 is only $-13dB$). A 7% frequency shift between simulation and measurement is observed: it can be ascribed to the average 5% tolerance of the commercial lumped element components and to the critic C_{LINK} dependence on the realized antenna pair geometry. Fig. 4.4 compares the link RF-to-RF transfer efficiency of the capacitive resonant link computed using the measured and simulated four-port scattering parameters, by the previously introduced equation (3.3).

The ideal η_{LINK}, computed with lossless components and dedicated networks optimized for each antennas distance, is also superimposed in Fig. 4.4: an improvement of only $3-4\%$ with respect to the simulated realistic situation is observed, which confirms that the proposed unique

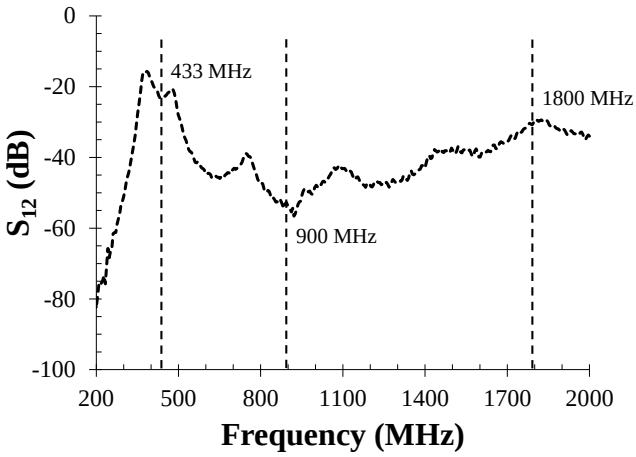

Figure 4.2: Measured isolation between ports 1 and 2 of Fig. 3.6 for the standalone antenna.

matching network can be effectively exploited. The measured efficiency shows a 10% degradation, which is mainly due to the lower Q-factor of the adopted commercial components.

Fig. 4.5 shows the measured RF-to-DC conversion efficiency of the rectifier (η_{RF-DC}) as a function of the received RF power (P_{OUT}^{WPT}), while Figs. 4.6 and 4.7 report the measured $\eta_{WPT-LINK}$ of the entire link and DC output power, respectively, as a function of the link input power (P_{IN}^{WPT}) with the antenna distance as a parameter: the shapes of these plots clearly show the non-linear behaviour of the rectifier. When the portable devices are located 1 cm apart, the measured RF-to-DC efficiency of the entire link, from the link input power port to the rectifier DC output is better than 20%, for a transmitted power of only $10\,dBm$, whereas for greater distances it goes below 10%. Of course, the use of strip-like antennas of different shape on each side of the link could bring to different performance, but not so far from those here presented: the effectiveness of this idea does not depend on the symmetry of the link, but on the creation of a weak reactive link between faced mobiles. As previously mentioned, the obtained WPT efficiencies are worse than

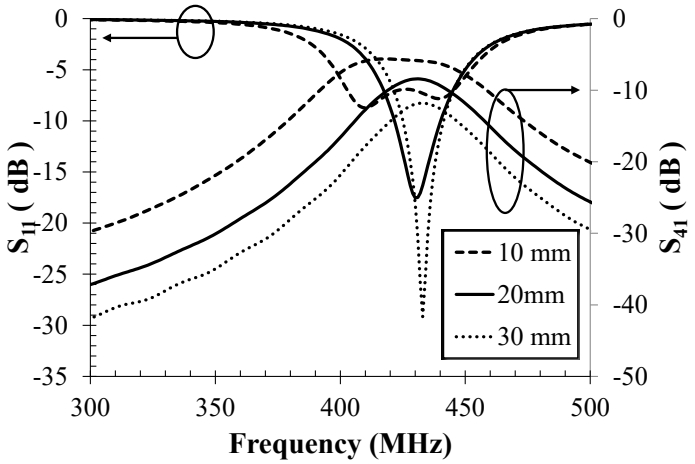

(a)

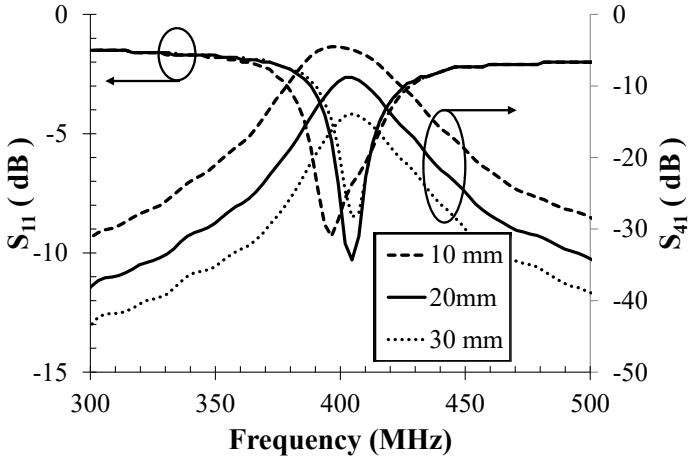

(b)

Figure 4.3: Simulated (a) and measured (b) reflection and transmission coefficients for the two faced antennas fed by the diplexer network (ports number as in Fig. 3.6).

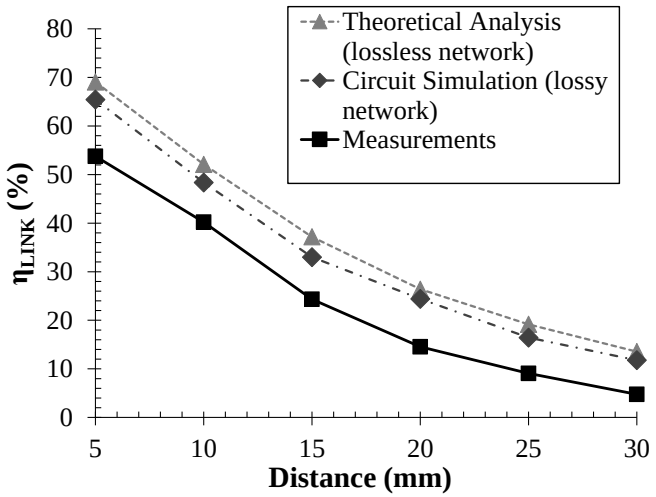

Figure 4.4: Predicted (with and without losses) and measured reactive link efficiencies for variable antenna distances, calculated through Eq. (3.3).

those offered in the literature by dedicated resonant links: the results here presented are given by already existing architectures, with a limited number of add-on components.

4.2 Simultaneous NF-FF operations

In this section, the purpose is to verify experimentally if WPT and communication operations can simultaneously exist. First the antenna fed by the diplexer is characterized at UHF in standalone conditions and faced to another one at the three distances previously considered: the measured reflection coefficient at the UHF port (port 2 in Fig. 3.6) of Fig. 4.8 shows that antenna matching is preserved. The measured normalized radiation patterns of Fig. 4.9 confirm that also the far-field properties are still guaranteed, even if they slightly worsen mainly for electromagnetic coupling reasons. This is also confirmed by the simulated antennas radiation efficiencies: from 98% and 96% at 900 MHz and 1800 MHz for the standalone antenna, to 45%, 52%, 59% and 54%,

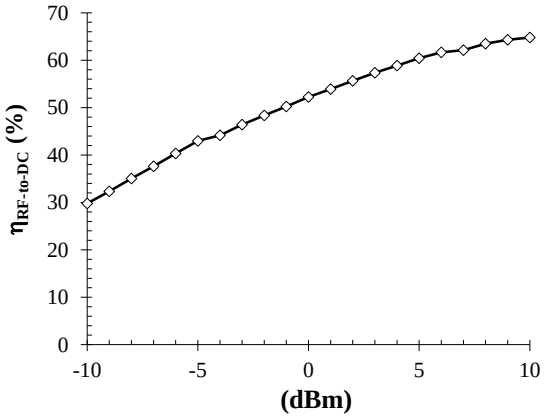

Figure 4.5: Measured RF-to-DC efficiency of the rectifier.

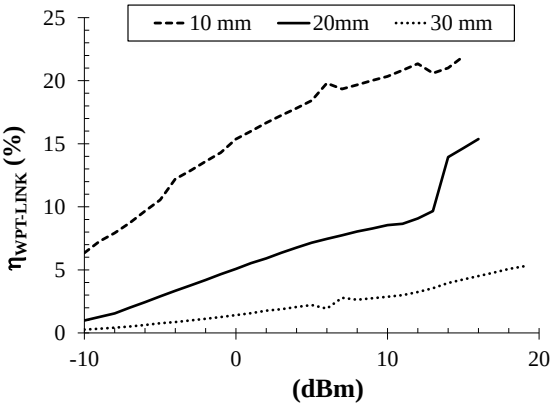

Figure 4.6: Overall system efficiency, from the link input power port to the rectifier DC output, for variable link distances.

61%, 73% in the two bands for the antennas faced at 10, 20, 30 mm, respectively.

Finally the experimental set-up of Fig. 4.10a has been arranged to measure the simultaneous near-field WPT and far-field data communication of the system of Fig. 3.6 for a 20-mm-distance between the

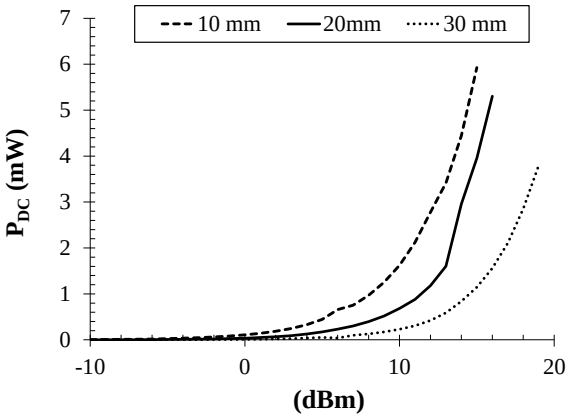

Figure 4.7: DC output power for variable link distances.

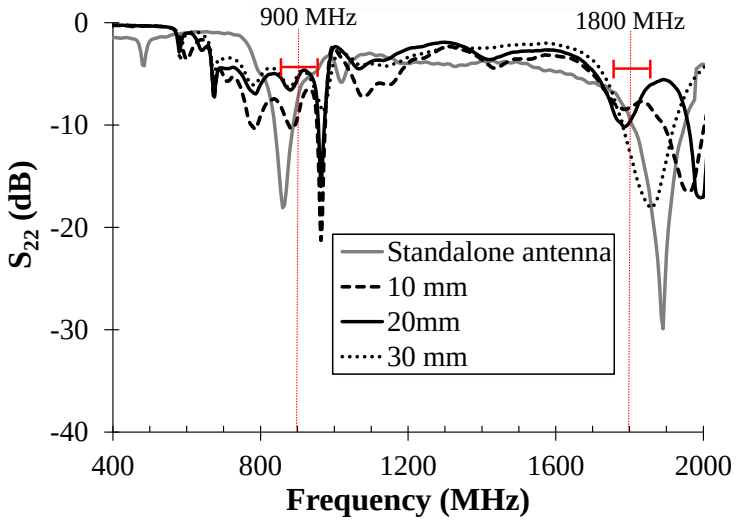

Figure 4.8: Input reflection coefficient at port 2 of Fig. 3.6, with standalone antenna and with a faced identical one, at different distances.

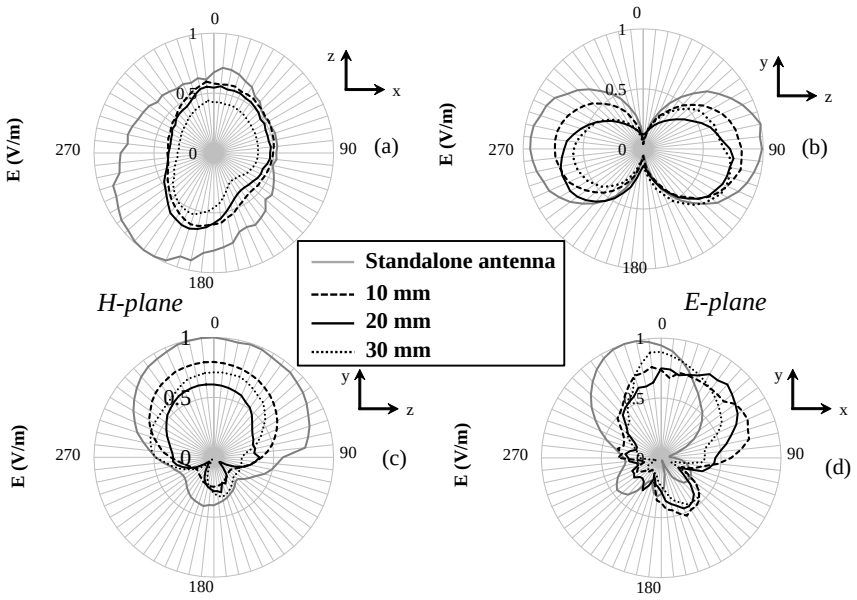

Figure 4.9: Antenna radiation patterns in H- and E- plane at 900 MHz ((a) and (b)) and 1800 MHz ((c) and (d)) (linear scale) for the standalone antenna and with a faced identical one, at different distances.

antennas. The WPT port of the first antenna (port 1) is connected to the signal generator at 403 MHz (the frequency with the best measured RF-to-RF transfer efficiency) while port 2 at UHF is connected to a 1800 MHz source of $-10\,dBm$. To severely test the system, the highest WPT input power ($10\,dBm$) is used. The corresponding power- and communication-ports of the second antenna are connected to the rectifier and to a $50\,\Omega$ termination, respectively. The radiated field is measured by a horn antenna, connected to a spectrum analyser, located at $1.5\,m$ distance from the experimental set-up. At the same time, the rectifier output voltage (V_{RECT}) is measured by means of a low-frequency oscilloscope. The two RF sources (WPT and UHF ones) are simultaneously active and the following quantities are monitored: i) the received far-field power spectrum at UHF for the standalone antenna and with the other one faced at 20-mm distance. This allows to account for antenna proximity effects on the communication performances, and thus

to validate the results of Figs. 4.84.9; ii) the received power spectrum at 403 MHz when the two antennas are close by, to verify the absence of radiation at this frequency that may interfere with other existing systems. This also validates the results of Fig. 3.5c; iii) the collected DC voltage at the rectifier output.

Fig. 4.10b compares the received signals in the absence and in the presence of the nearby antenna: a signal strength reduction of $6dB$ need be accounted for if the second antenna is closely located for WPT purposes, confirming that communication is still possible during energy transfer; Fig. 4.10d shows the received power spectrum in the WPT band: a level lower than$-70dBm$ is measured, ensuring that the sole near-field is involved in the power transfer operation, hence no spurious interference with other devices operation takes place. Finally the transient behaviour of the rectifier DC output voltage is measured in the same set-up conditions, and is reported in Fig. 4.10c: a 1.8 V peak is reached after a charging time of $50\mu s$, on a $10\mu F$ storage capacitor.

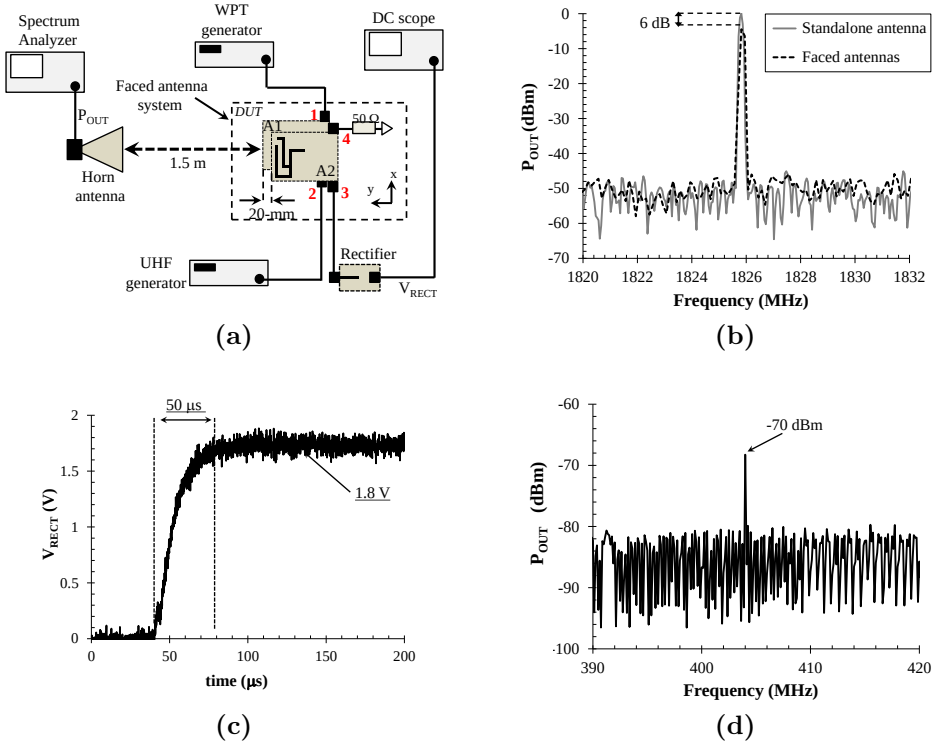

Figure 4.10: (a) Block-representation of the measurement set-up with the faced antennas at 20 mm distance. (b) Received normalized power spectra at 1800 MHz, radiated; (c) charging transient of the WPT rectifier output on a $10\mu F$ storage capacitor; (d) received normalized power spectrum in the WPT band radiated by the antenna faced to an other one.

Chapter 5

Space Mapping Technique

With this Chapter, as mentioned at the beginning of the thesis, I will present and explain the topic I focused on as a visiting researcher at the Institute of Microwave and Photonic Engineering (IHF) at the Graz University if Technology (Graz, Austria) for my PhD period abroad. In particular, this topic is not related to SWIPT applications, but it is again related to energy-aware solutions, being the energy saving the core of my job. In this activity, passive Radio frequency identification (RFID) sensor transponders (tags) backscattering is deployed for retrieving information on the environment surrounding the tag

5.1 Introduction

Radio frequency identification (RFID) sensor transponders (tags) provide low-cost, low-maintenance sensing capabilities, thus offering, for various Internet of Things (IoT) applications, an attractive alternative compared to power consuming active sensor nodes. In the field of RFID sensor tags, one of the proposed methods in literature is to use the RFID antenna itself as an environment sensing device [66, 67, 68]. Nowadays, the antenna design is mainly based on full-wave electromagnetic simu-

lations. Several numerical methods are widely used, but they require a large number of computational resources especially for high frequencies. In addition, simulation-driven design is a challenging task. In fact, it consists of time consuming parameter sweeps guided by the problem solving knowledge of the specific designer. Significant reduction of the computational cost has been demonstrated using adjoint sensitivity-based geometry evolution [69] or surrogate-based optimization methods [70]. Several techniques have been developed in recent years, but the most popular in microwave and antenna engineering is the space mapping technique [71]. The space mapping technique is based on two distinct models, i.e., a coarse circuit model (CM) and a corresponding fine electromagnetic model (EM) [71], and it is adopted in this work to derive the antenna model exploited as a transducer of different bending configurations. The coarse CM is based on the circuit simulator AWR [3], while the fine EM is obtained by the electromagnetic simulator CST [2]. The CM allows in a time efficient way an initial antenna transducer design, while the EM is used to finalize the generated topology before antenna prototyping [71, 72]. In previous works [68, 73, 74], the antenna design for RFID sensor tags has been realized combining circuit electromagnetic analysis and Matlab for the optimization. In the following pages, I will deeply explain a space mapping idea that has been simply represented through the block diagram in Fig. 5.1: starting from an initial geometrical layout of a T-matched antenna simulated in CST [2] (*initial EM*), I will find its input impedance equivalent model, represented through lumped elements, into AWR [3] simulator (*initial CM*). Therefore, I will implement an algorithm that will exploit the initial CM and a specific figure of merit in order to find out the best lumped element representation of our ideal target (*final CM*). Once completed

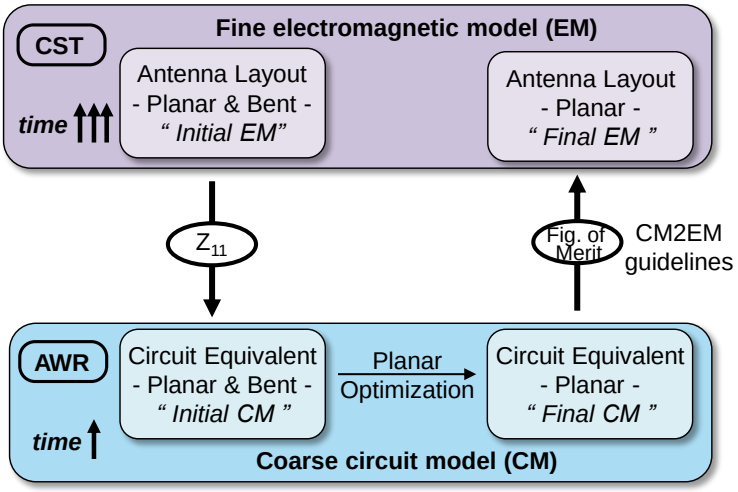

Figure 5.1: Space Mapping idea represented through block diagram. For Simulators here represented, refer to [2] for CST and to [3] for AWR.

the optimization, I will need to convert again my final lumped element CM into a geometrical layout (*final EM*) for a final verification of the achieved results. In this way I will exploit a combination of the CM analysis and EM simulation, in order to take advantage of the speed of the former and the accuracy of the latter, with the goal of implementing a space mapping design method for an antenna transducer of a bending sensor RFID tag.

The time-efficient CM is exploited in order to redesign an initial antenna layout in order to respect specific design goals driven by a figure of merit. In the next pages, an innovative figure of merit for RFID sensors will be introduced, explained and adopted. To conclude, some design guidelines are also shown to help in converting the CM final layout into an EM with a final comparison between the expected figure of merit from the CM and the more accurate one obtained with the EM.

5.2 Antenna Transducer

In RFID sensor tag concept, exploiting the antenna itself as a transducer, has been first considered in [68] for sensing liquid filling. In this work, we design an antenna transducer using a passive ultra-high frequency (UHF) RFID tag for antenna bending states sensing: possible applications could be a movements monitor of a robotic arm made of non-metallic materials or of a prosthesis. The antenna transducer is based on a T-matched dipole antenna (see Fig.5.3a), which has been demonstrated to be a suitable antenna transducer for a UHF RFID sensor tag [68, 75]. The central operating frequency is 868 MHz, while the band used to derive the CM ranges from 840 to 890 MHz. This allows to ensure a safety range of accuracy over the whole European UHF RFID frequency band.

In this work, the sensor tag aims to sense two discrete states with bending radii of $R_{b1} = 80\,mm$ and $R_{b2} = 37.5\,mm$ (see Fig.5.3b). In general, it is possible to sense also more than two sensing states, but we have to consider that, increasing the number of sensing states (K from now), increases the complexity of the antenna transducer design. In addition, the number of sensing states (K) is limited by the noise in the RFID communication system. If the noise at the reader side is too high, the correct detection of the sensor tag could be compromised.

5.2.1 RFID concept

A tag antenna and the RFID chip can be characterized by their impedances, i.e., by the antenna impedance $Z_{Ant} = R_{Ant} + jX_{Ant}$ and by the chip impedance in the absorbing mode$Z_{Abs} = R_{Abs} + jX_{Abs}$ and the chip impedance in the reflecting mode $Z_{Ref} = R_{Ref} + jX_{Ref}$. The antenna and chip impedances of state-of-the-art UHF RFID tags are

typically optimized to ensure a reliable power transfer from the tag antenna toward the tag chip and to ensure a reliable tag ID transmission toward the RFID reader. The tag signal is thus amplitude modulated by switching between the chip absorbing and reflecting impedances, i.e., representing a logical "0" by an increased power absorption by the chip and a logical "1" by an increased power reflection at the chip input. The backscattered tag signal at the chip input is related to the reflection coefficients in the absorbing mode S_{Abs} and in the reflecting mode S_{Ref} that are defined as follows by the antenna and chip impedances [76]:

$$S_{Abs} = \frac{Z_{Abs} - Z_{Ant}^*}{Z_{Abs} + Z_{Ant}} \quad , \quad S_{Ref} = \frac{Z_{Ref} - Z_{Ant}^*}{Z_{Ref} + Z_{Ant}} \tag{5.1}$$

A measure for the power absorption, or rather the chip power supply, is the power transmission coefficient τ that is defined as $\tau = 1 - |S_{Abs}|^2$ [27]. In the absorbing mode, τ is ideally 1. In the reflecting mode, τ is ideally 0, i.e., the signal is totally reflected at the chip input.

5.2.2 Figure of Merit

A useful figure of merit to be adopted for the antenna design is the sensor tag efficiency introduced in [68] that allows to quickly evaluate the quality of an antenna transducer when connected with a specific RFID chip. The sensor tag efficiency α is defined in the following expression:

$$\alpha = \sqrt{\alpha_1 \cdot \alpha_2 \cdot \alpha_3} \tag{5.2}$$

and this figure of merit remains within the range $0 \leq \alpha \leq 1$, where $\alpha = 1$ is obtained only when an ideal transducer design is obtained.

From (5.2) it can be observed that three factors contribute to the overall figure of merit.

The first term of (5.2) describes the phase configuration of the absorbing reflection coefficient and provides information about the quality of the phase modulation when a maximization of the phase shift between the different involved sensing states (Δ_k) is desirable. In particular, α_1 defines the sensing state transmission efficiency defined in the following way:

$$\alpha_1 = \frac{\Delta\phi_{Min}}{360/K} \tag{5.3}$$

which is a function of the minimum phase difference $\Delta\phi_{Min}$ (in degrees) of the reflection coefficients in the absorbing mode at each sensing state $S_{Abs}(\Delta_k)$. As normalization factor for $\Delta\phi_{Min}$, in (5.3) it has been proposed to use the ideal value the K sensing state investigated (360°/K) in order to highlight how far the configuration is from the ideality ($\alpha_1 = 1$).

The second term of (5.2), α_2, describes the amplitude configuration of the absorbing reflection coefficients and thus provides information about the power supply of the passive RFID chip. Thus, α_2 defines the power transfer efficiency and is defined as follows:

$$\alpha_2 = 1 - \beta_1 |\tau_{ref} - \tau(\Delta_k)|_{Max} \tag{5.4}$$

which is a function of the maximum deviation of the power transmission coefficient $\tau(\Delta_k)$ in each sensing state from a specified reference value τ_{ref}, i.e., a function of the maximum absolute difference of $\tau(\Delta_k)$ and τ_{ref}. Equation (5.4) must follow the restriction that $|\tau_{ref} - \tau(\Delta_k)|_{Max} \leq 1/\beta_1$, where β_1 is a weighting factor that lies within

$0 \leq \beta_1 \leq 10$. The weighting factor β_1 is used to balance the influence of the power transfer efficiency α_2 on α. A small value of β_1 decreases the influence of α_2 on the sensor tag efficiency, while a high value of β_1 increases the influence of α_2 on α.

Regarding α_3, the third term of equation (5.2), it is useful when two sensing states are investigated and takes into account the quality of the tag signal. Indeed, this factor takes into account the amplitude difference between reflection coefficient in absorbing mode and in reflecting mode for each sensing state. In particular, α_3 is defined as follows:

$$\alpha_3 = 1 - \beta_2 |\eta_1 - \eta_2| \tag{5.5}$$

which is a function of the modulation efficiency defined as $\eta_i = (2/\pi^2)\,|S_{Abs_i} - S_{Ref_i}|^2$ $(i = 1, 2)$ [77]. A maximum modulation efficiency of about $\eta = 0.2$ can be realized for an amplitude-modulated tag signal. In addition, there is here also β_2 as a factor that helps in weighting this contribute with respects to the others above introduced (α_1 and α_2). Regarding equation (5.5), it is important to follow the restriction of $|\eta_1 - \eta_2| \leq 1/\beta_2$, strictly related to β_2 that can lie within the same range of β_1.

Thanks to the previous paragraph, it is then possible to write an extended version of equation (5.2) as in the following:

$$\alpha = \sqrt{\frac{\Delta\phi_{Min}}{360/K} \cdot (1 - \beta_1 |\tau_{ref} - \tau(\Delta_k)|_{Max}) \cdot (1 - \beta_2 |\eta_1 - \eta_2|)} \tag{5.6}$$

where K is the number of sensing states, β_i are weighting factors between the phase and amplitude power transfer and τ_{ref} is the power transmission coefficient we want to achieve. For any bending state, the

sensor tag efficiency is a function of the antenna input impedances Z_{Ant} and of the chip impedance in the tag absorbing mode (i.e., $Z_{Abs} = (20 - j180)\,\Omega$ [78]). Here-hence, it is possible to calculate $\Delta\phi_{Min}$, in degrees, as the minimum phase difference of the reflection coefficients in the absorbing mode at each sensing state $S_{Abs}(\Delta_k)$ and $\tau(\Delta_k)$ is the power transmission coefficient at each sensing state k, with $k = 1, 2$.

Thus, an efficient antenna transducer can be realized by correlating different antenna impedances to different bending states with the goal of maximizing the sensor tag efficiency.

5.3 Circuit Model

By means of both the circuit equivalent model of the antenna impedance with respect to either flat or bent states, and the RFID chip impedances a rapid exploration of the T-matched dipole and its sensor tag efficiency can be quickly evaluated. With this purpose, a circuit model is necessary in order to pass from an initial EM to the initial CM. For a better understanding, the step of the space mapping illustrated in Fig. 5.1 that is explained in this section is illustrated in Fig. 5.2.

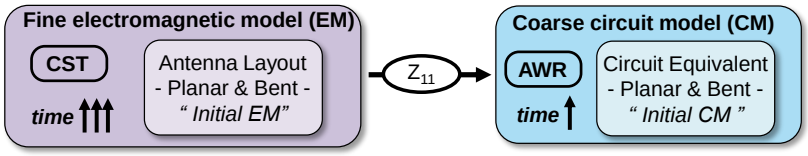

Figure 5.2: For a clear comprehension, here is shown the part of the Block Diagram shown in Fig. 5.1 explained in this section.

For this reason, a CM of the flat T-matched dipole is derived and it is shown in Fig. 5.4, starting from the topology adopted in [75]. The proper lumped elements values are also shown in the same figure. It is possible to relate the antenna states, schematically represented in Fig.

5.3, and the adopted CM shown in Fig. 5.4 [75]. The left part of the CM ($R0_a$, $C0_a$, $L0_2$) models the T-match feeding network (whose geometry is given by L_2, L_3, W_2,W_3), whereas the right part of the CM ($R0_t$, $C0_t$, $L0_1$) models the dipole (whose geometry is given by L_1, W_1). The coupling between the dipole and T-matched network is modelled by the transformer in the CM. This information will be the basis for the space mapping design method.

Then, for any bending state, the CM models are built by introducing extra lumped elements, that are highlighted in blue in Fig. 5.5. The real and imaginary antenna impedances computed by EM simulation of the flat and bent antenna are shown in Figs. 5.6 and 5.7, respectively. These simulations show a non-monotonic variation of the antenna resonance frequency versus different bending states (namely, for radii equal to 75, 250 and 500 mm). To account for this behaviour, the series connection $R0_a$, $C0_a$ of Fig. 5.4 is replaced by a series connection of parallel-connected resistances and capacitances branches. In this way, the overall resistance model can span from short circuit (SC) to open circuit (OC), starting from R_{ap} open and R_{as} short.

In this way, an accurate modelling of the T-matched antenna resonance frequencies with respect to the bending states has been obtained. This analysis has been carried out also for extra bending states besides the targeted ones (i.e., with bending radii of 50, 75, 100, 150, 250 and 500 mm).

The final CM parameters are derived by means of optimization to fit the T-matched dipole input impedances derived from the EM analyses of the bending structures, with the goal of minimizing the relative errors between the EM and CM, for all the considered bending states. Again, the antenna impedance is used as target:

$$e_r = |\frac{Z_{AntCM}(f) - Z_{AntEM}(f)}{< Z_{AntCM}(f),\, Z_{AntEM}(f) >}| \tag{5.7}$$

where $Z_{AntCM}(f)$, $Z_{AntEM}(f)$ should be substituted by the corresponding real and imaginary counterparts.

This design procedure allows to reach a very good CM approximation of the initial planar and bended T-matched dipole within the adopted range of interest of [840-890 MHz]: the maximum relative error is lower than 14% and 0.8% for the real, $Re(Z_{Ant})$ (see Fig. 5.8) and $Im(Z_{Ant})$ imaginary (see Fig. 5.9) parts of the antenna impedance, respectively.

In addition, the optimized topology of Fig. 5.5 achieves a very small relative error, at the frequency of interest of 868 MHz, with respect to the EM model in all the investigated bending states, the maximum being 5.9% for the $Re(Z_{Ant})$ (see Fig. 5.8) and 0.03% for the $Im(Z_{Ant})$ (see Fig. 5.9), respectively. Thus, it can be concluded that the obtained circuit model can be safely adopted in place of the EM model for further evaluations of the antenna sensor tag performance, such as the sensor tag efficiency. In this way the geometrical parameters of the antenna itself can be modified according to their corresponding circuit equivalent values. For example, using the CM model of the bent T-matched antenna, the more suitable impedance states can be computed as those which ensure the highest sensor tag efficiency ($\alpha = 1$) in terms of real and imaginary parts of the antenna impedance.

For example, in Table 5.2 we can see the impedances of the adopted initial layout (Fig. 5.3) for the two bending configurations under exam (column "Actual"). In the same table, labelled as "Ideal", the suitable impedances that the two sensing states must have in order to ensure a maximum sensor tag efficiency ($\alpha = 1$) are also listed. The differences between these impedances, are then listed in the last column of Table

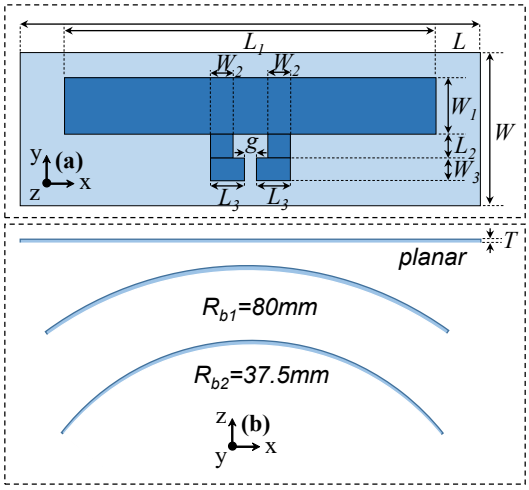

Figure 5.3: (a) layout of the T-matched dipole with its geometrical parameters whose values are: $L = 119$, $W = 51$, $L1 = 80$, $W_1 = 12$, $L_2 = 6$, $W_2 = 5$, $L_3 = 8.5$, $W_3 = 5$, $T = 0.075$, $g = 2$, $t_{metal} = 0.035$. All dimension are in mm. (b) bending states.

5.2 in terms of percent deviation for both the real and imaginary parts. Starting from the ideal antenna impedance values, Fig. 5.11 shows a map of the sensor tag efficiency as computed in [68] and reported in (5.6), with respect to percent deviations from the ideal real and imaginary parts of the antenna impedances in the three bending states. From Fig. 5.11 it can be seen that to ensure a sensor tag efficiency higher than 80% it is necessary to obtain an antenna whose impedances, for the different states, deviate from the ideal ones less than $\pm 16.6\%$ and $\pm 1.2\%$ for $Re(Z_{Ant})$ and $Im(Z_{Ant})$, respectively. For the initial CM design we can notice how far we are to satisfy the final values.

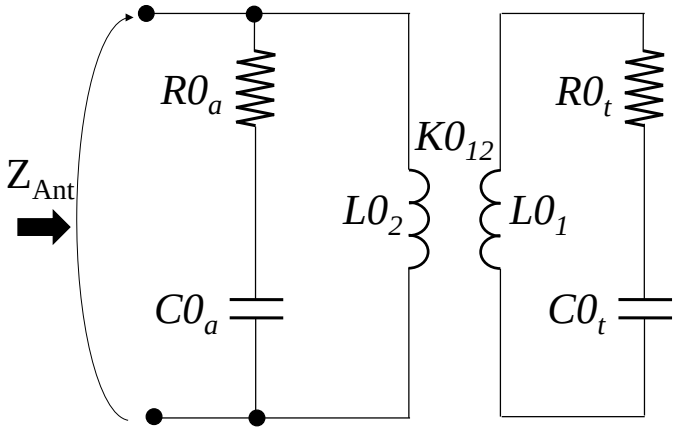

Figure 5.4: Equivalent circuit of the planar T-matched dipole. The lumped elements for the initial CM are: $R0_a = 0.51\,[\Omega]$, $C0_a = 5.80 \cdot 10^{-7}\,[\mu F]$, $R0_t = 56.83\,[\Omega]$, $C0_t = 0.98 \cdot 10^{-3}\,[\mu F]$, $L0_1 = 303.09\,[nH]$, $L0_2 = 16.48\,[nH]$, $K0_{12} = 0.494\,[\,]$.

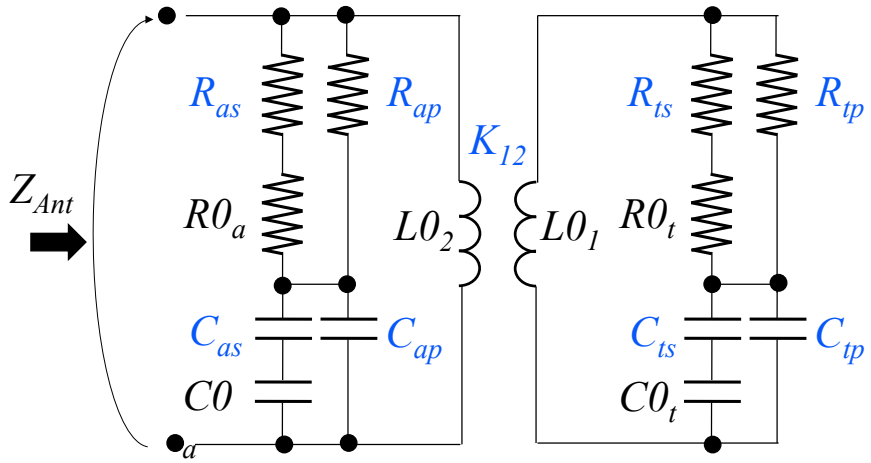

Figure 5.5: Modified equivalent circuit of the T-matched dipole to account for bending states. The lumped elements related to the planar geometry (in black) are listed in the caption of Fig. 5.4, the extra elements (in blue) values, depending on bending are listed in Table 5.1.

Table 5.1: Parameters of the CM shown in Fig. 5.5 for two different bending radii: $R_{b1} = 80\,mm$ and $R_{b2} = 37.5\,mm$. The acronym SC and OC represent a short and open circuit, respectively.

Parameter	R_{b1}	R_{b2}
$R_{as}\,[\Omega]$	180.23	1.68
$R_{ap}\,[\Omega]$	OC	OC
$C_{as}\,[\mu F]$	$2.07 \cdot 10^{-7}$	$10.08 \cdot 10^{-7}$
$C_{ap}\,[\mu F]$	OC	OC
$R_{ts}\,[\Omega]$	SC	SC
$R_{tp}\,[\Omega]$	105.24	95.45
$C_{ts}\,[\mu F]$	$9.33 \cdot 10^{-7}$	$8.98 \cdot 10^{-4}$
$C_{tp}\,[\mu F]$	OC	OC
$K_{12}\,[\,]$	0.529	0.482

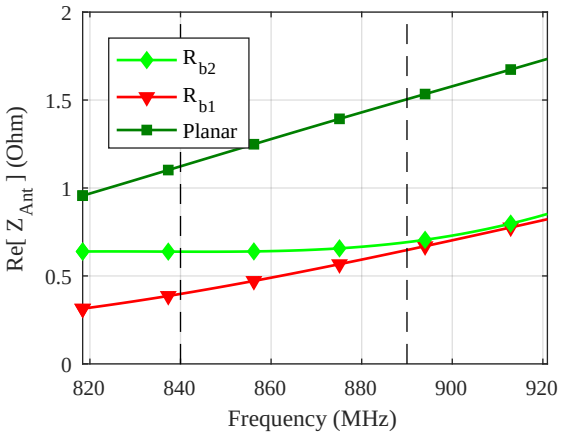

Figure 5.6: $Re(Z_{Ant})$ of the EM for the planar T-matched dipole and the T-matched dipole for the three bending states, $R_{b1} = 80\,mm$ and $R_{b2} = 37.5\,mm$. Vertical dotted lines point out the frequency band of interest for the CM optimization (840-890 MHz).

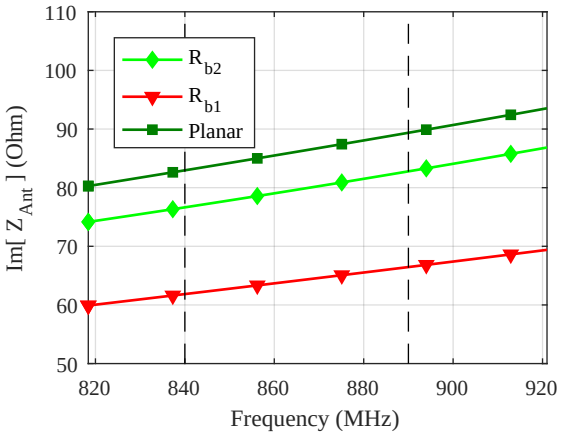

Figure 5.7: $Im(Z_{Ant})$of the EM for the planar T-matched dipole and the T-matched dipole for the three bending states, $R_{b1} = 80\,mm$ and $R_{b2} = 37.5\,mm$. Vertical dotted lines point out the frequency band of interest for the CM optimization (840-890 MHz).

Table 5.2: "Actual" values adopted for the two bended states computed with initial CM model adopted and compared with respect to "Ideal" values that can ensure the highest sensor tag efficiency ($\alpha = 1$).

Ant. imp.	*Actual*		*Ideal*		*Rel. difference*	
$[\Omega]$	Re	Im	Re	Im	$\Delta Re\,\%$	$\Delta Im\,\%$
$Z_{Ant\,1}$	0.6463	79.89	16.62	320.2	185	120
$Z_{Ant\,2}$	0.5251	64.37	16.62	329.7	187	134

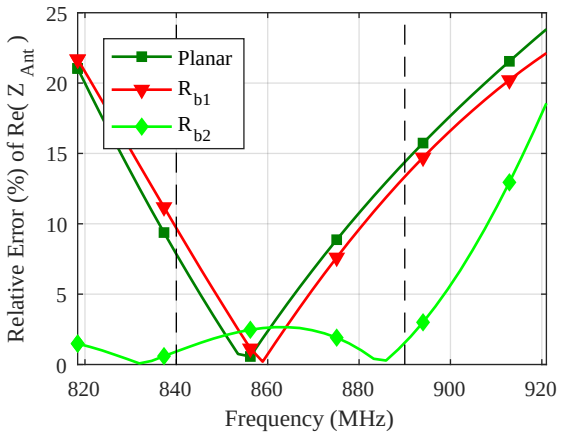

Figure 5.8: Relative error of $Re(Z_{Ant})$ of the planar T-matched dipole and the T-matched dipole for the three bending states, $R_{b1} = 80\,mm$ and $R_{b2} = 37.5\,mm$. Vertical dotted lines point out the frequency band of interest (840-890 MHz).

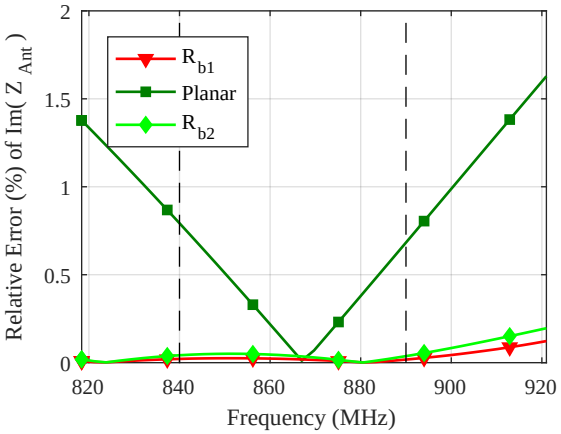

Figure 5.9: Relative error of $Im(Z_{Ant})$ of the planar T-matched dipole and the T-matched dipole for the three bending states, $R_{b1} = 80\,mm$ and $R_{b2} = 37.5\,mm$. Vertical dotted lines point out the frequency band of interest (840-890 MHz).

5.4 Optimization

5.4.1 Algorithm implementation

Referring to Fig. 5.1, the optimization I will explain in this Chapter is the automatic way implemented in AWR [3] environment that allows to exploit the circuit model introduced in the previous Chapter and to modify it thorough the maximization of a figure of merit that can numerically represent the desired project goals. In particular, the figure of merit here adopted is the sensor tag efficiency that has been deeply previously explained. For a better understanding, the step of the space mapping illustrated in Fig. 5.1 that is explained in this section is shown in Fig. 5.10.

The algorithm implemented in AWR [3], requires to design the initial CM for each of the investigated bending states. In my case, I have designed a CM of the topology shown in Fig. 5.5 with the specific lumped element values reported in Table 5.1 for each of the two analysed bending radii. This can be assumed as the starting point for the optimization process.

As a second step, a script that calculates the sensor tag efficiency has been implemented in AWR [3] using the Output Equations feature. Output equations assign the result of a measurement to a variable, which can be used in other equations just like other variables. A project can include multiple Output Equations documents, each of which can con-

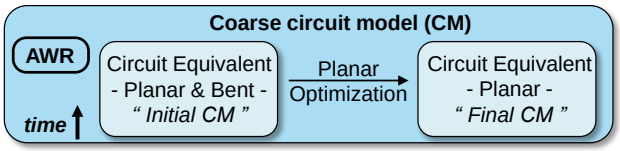

Figure 5.10: For a clear comprehension, here is shown the part of the Block Diagram shown in Fig. 5.1 explained in this section.

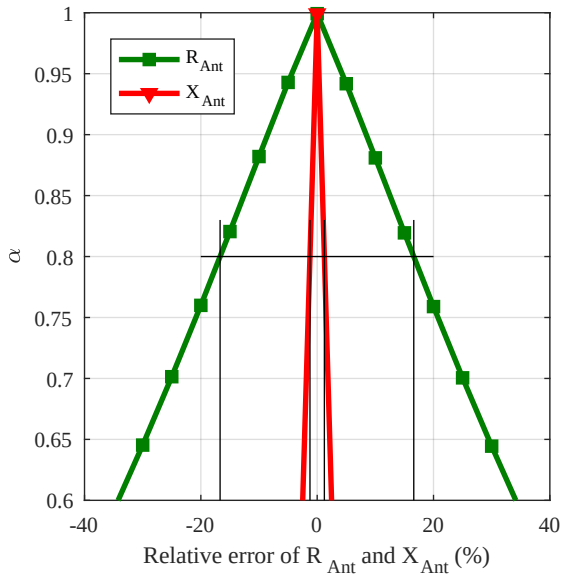

Figure 5.11: Sensor tag efficiency versus the relative error of $Re(Z_{Ant})$ and $Im(Z_{Ant})$, respectively.

tain multiple output equations and standard equations. Note that the term "output equations" refers to both: the type of document, and the type of equations that can be added in those documents. In Fig. 5.12 the sensor tag efficiency (5.6) calculation implemented in AWR [3] is reported.

Apart the figure of merit definition, other constraints were necessary. In particular, I needed to limit the amplitude of scattering parameters obtained during the optimization process (i.e., $0 \leq S_{Abs_{Rbi}} \leq 1$ for $i = 1, 2$) in order to get physically meaningful final results.

Regarding the adopted “rules”, another part is still missing. Indeed, the optimization process requires also the definition of some “goals” that AWR [3] uses as cost function of the overall optimization. In my case, the main goal was the maximization of the figure of merit (sensor tag efficiency, α), defined in equation (5.6) and implemented as shown in Fig. 5.12, at the specified 868 MHz frequency of interest.

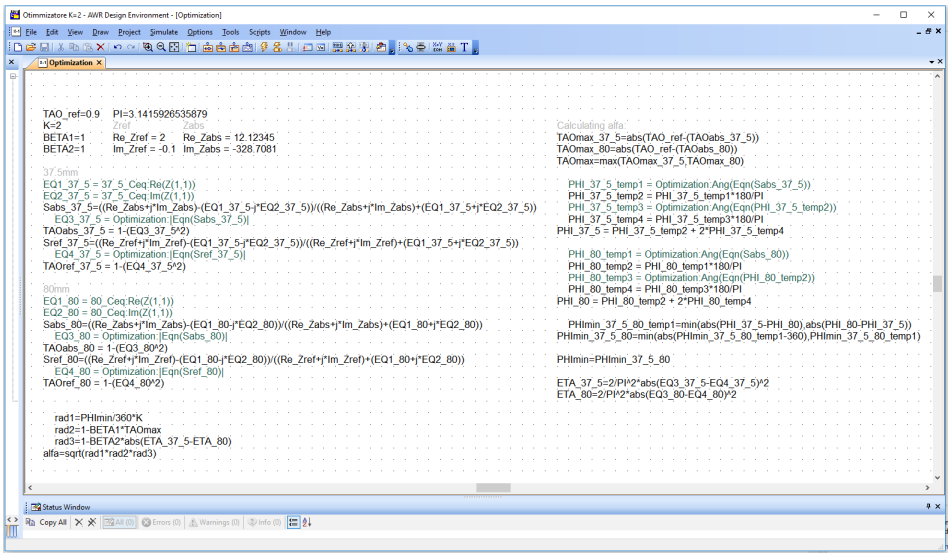

Figure 5.12: Sensor tag efficiency (5.6) calculation implemented in AWR [3] for the optimization step illustrated in Fig. 5.10.

The initial CM, described with parameters listed in Table 5.1, shows an initial estimation of the sensor tag efficiency of 0.62% only. This result is really low but, considering the values of relative difference listed in Table 5.1, this is what I expected.

Considering that my goal is to optimize the antenna layout in order to find out the best geometry that allows to maximize the sensor tag efficiency at the two investigates bending radii ($R_{b1} = 80\,mm$ and $R_{b2} = 37.5\,mm$), the optimization uses the lumped elements that describe the planar configuration of the antenna, only (see Fig. 5.4) whereas the parameters that represent the bent configurations remain fix (refer to the blue lumped elements represented in Fig. 5.5). Thanks to this optimization, a sensor tag efficiency of about 95.53% has been achieved as shown in Fig. 5.13.

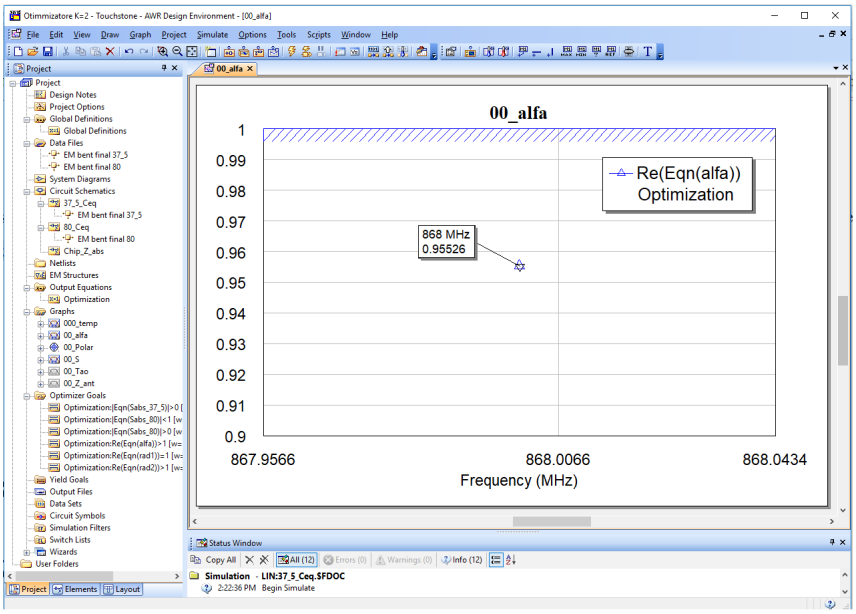

Figure 5.13: Screenshot of the high sensor tag efficiency obtained at the end of the optimization process.

5.4.2 Final CM

Thanks to the just described optimization, it has been possible to achieve a sensor tag efficiency of about 95.53% (see Fig. 5.13). The final planar CM lumped element values and their variations with respect to the initial planar CM are listed and expressed in percentage in Table 5.3. In particular, it is important to mention that the aim of Table 5.3 is only to show which parameters of the final planar CM of Fig. 5.4 are incremented (or reduced) with respect to the initial CM without focusing on the order of magnitude. In fact, it is observable how some parameters (i.e $R0_a$ and $R0_t$) show an excessive increment.

Now, in order to proceed with overall space mapping technique, it is necessary to find a relation between the variations of the lumped elements listed in Table 5.3 and some of the possible geometrical parameters that represent the layout of Fig. 5.3a. This aspect is investigated in the following paragraph.

Table 5.3: Parameters list of both initial and final planar CM shown in Fig. 5.4. In addition, the relative difference of the final value with respect to the initial one expressed in percentage is highlighted in the last column.

Parameter	*Final CM*	*Initial CM*	*Rel. difference* [%]
$R0_a\,[\Omega]$	20.08	0.51	$+3'845\%$
$C0_a\,[\mu F]$	$4.93 \cdot 10^{-7}$	$5.80 \cdot 10^{-7}$	-15%
$R0_t\,[\Omega]$	$989'670$	56.83	$+175'251\%$
$C0_t\,[\mu F]$	$1.91 \cdot 10^{-3}$	$0.98 \cdot 10^{-3}$	$+91\%$
$L0_1\,[nH]$	153.06	303.09	-51%
$L0_2\,[nH]$	32.80	16.48	-99%
$K0_{12}\,[\,]$	0.499	0.494	$+1\%$

5.5 Back to EM

5.5.1 CM to EM guidelines

In order to pass from the planar final CM to its equivalent representation using an EM, it is necessary to have some guidelines that can help the designer in the modification of the right geometrical parameters in the right direction (i.e. decrease or increase a specific lumped element). In particular, referring to Fig. 5.1, the part explained in this section is highlighted in Fig. 5.14 for a clearer comprehension.

With this goal in mind, the idea is to progressively increase and decrease each of the possible geometrical parameters of the planar layout (Fig. 5.3) and calculate the corresponding CM (Fig. 5.4) for each modified geometry. Therefore, the designer has to proceed with the comparison of these lumped elements, representative of each geometrical variation, with respect to the lumped elements obtained with the initial unmodified layout. Indeed, we can generally expect that, when a geometrical parameter is changed with respect to an initial configuration, the modification is reflected on more than one lumped element. For this reason, it is important to identify for each "modified geometry" those lumped elements that imply an increase or a decrease of the geometrical parameter and possibly at the same time characterize only one geometric variation. This second aspect is essential in order to univocally associate a lumped element variation to a single geometrical parameter variation.

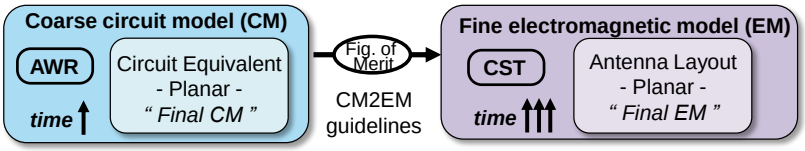

Figure 5.14: For a clear comprehension, here is shown the part of the Block Diagram shown in Fig. 5.1 explained in this section.

In particular, referring to Fig. 5.3a, the geometrical parameters that describes the initial adopted configuration for this investigation are $L_1 = 80\,mm$, $W_1 = 12\,mm$, $L_2 = 6\,mm$, $W_2 = W_3 = 5\,mm$ and $L_3 = 8.5\,mm$. For the unspecified parameters, please refer to caption of Fig. 5.3.

In Table 5.4 the percentage variation for the geometrical parameters and corresponding simulation name used in this analysis are shown. Generally, both the increase and the reduction have been considered for all parameters. In particular, due to geometrical limitation, it was not possible to decrease L_3 and, for this reason, higher values than the starting one have been considered for this parameter, only. Note that the percentage variation is not the same for all the terms, but the overall average remains approximatively around $\pm 40\%$. Once again, the only exception is $L_3$where we can observe an increment of 90%. In addition, each simulation name shows the name of the geometrical parameter involved and a subscript to indicate that has been increased (*"u"*) or decreased (*"d"*) with respect to its initial value.

As introduced above, for both the initial planar configuration (whose geometrical parameters are expressed in caption of Table 5.4) and all the "modified" simulations listed in Table 5.4, the equivalent CM of the type of Fig. 5.4 has been retrieved. The lumped elements obtained for the initial configuration are listed in the caption of Table 5.5 and used as normalization values to express the percentage variation of the lumped elements resulting from each modified layouts. As anticipated, the variations of the lumped elements univocally associated to a specific geometric variation are listed in Table 5.5. In particular, it is important to note that the sign of the lumped element variation reported in Table 5.5 allows to correctly guide the designer toward the decision of increasing or decreasing the specific parameter under exam.

Table 5.4: Geometrical parameter variations expressed in percentage with respect to the initial planar configuration of $L_1 = 80\,mm$, $W_1 = 12\,mm$, $L_2 = 6\,mm$, $W_2 = W_3 = 5\,mm$ and $L_3 = 8.5\,mm$ with respect to Fig. 5.3a.

Name	L_1 [%]	W_1 [%]	L_2 [%]	$W_2 = W_3$ [%]	L_3 [%]
#L1u	+25%	···	···	···	···
#L1d	−25%	···	···	···	···
#W1u	···	+33%	···	···	···
#W1d	···	−33%	···	···	···
#L2u	···	···	+50%	···	···
#L2d	···	···	−50%	···	···
#W2u	···	···	···	+40%	···
#W2d	···	···	···	−40%	···
#L3u	···	···	···	···	+90%

Table 5.5: Lumped elements variations expressed in percentage with respect to lumped elements values that represents the initial planar configuration. Initial values used for normalization are the following: $R0_a = 0.73\,[\Omega]$, $C0_a = 4.38 \cdot 10^{-7}\,[\mu F]$, $R0_t = 208.74\,[\Omega]$, $C0_t = 0.37 \cdot 10^{-3}\,[\mu F]$, $L0_1 = 177.85\,[nH]$, $L0_2 = 16.48\,[nH]$ and $K0_{12} = 0.569\,[\,]$ with respect to CM of Fig. 5.4.

Sim. Name	$R0_a$ $[\Omega]$	$C0_a$ $[\mu F]$	$R0_t$ $[\Omega]$	$C0_t$ $[\mu F]$	$L0_1$ $[nH]$	$L0_2$ $[nH]$	$K0_{12}$ $[\,]$
#L1u	249%	···	−43%	···	···	3.66%	···
#L1d	−100%	···	184%	···	···	−7.32%	···
#W1u	···	2.87%	···	···	···	···	···
#W1d	···	−0.76%	···	···	···	···	···
#L2u	···	···	104%	−99%	···	···	−59%
#L2d	···	···	−92%	+166%	···	···	28%
#W2u	···	26%	−15%	···	···	−26%	···
#W2d	···	−22%	21%	···	···	32%	···
#L3u	···	···	···	···	−100%	107%	···

5.5.2 Final EM

In this section, it will be explained how to get the final EM for the planar layout starting from the final CM obtained at the end of our optimization process.

The ingredients I need for this purpose are the initial planar CM,

the final planar CM (whose parameters are listed in Table 5.3) and the guidelines to pass from a CM to an EM (in particular Table 5.4 and Table 5.5) explained in the previous chapter.

Starting from the differences between the final and initial planar CM, it is possible to highlight a percentage variation of this differences as listed in Table 5.3. Such values are necessary only for having an idea of which lumped elements of the final CM represented in Fig. 5.4 are incremented (i.e. $R0_a$, $R0_t$, $C0_t$, $K0_{12}$) and which are reduced (i.e. $C0_a$, $L0_1$, $L0_2$) with respect to the initial CM. Now the next step requires to mark in Table 5.5 the same variation (in terms of sign) for all the parameters. The result of this step, is that most of the parameters are marked both in the increase (subscript *"u"*) and the decrease (subscript *"d"*) direction of respective simulations. Since the direction of the modification of a parameter has to be unique (or incremented or reduced) I decided to choose the direction that has more marks. In particular, this has to be done for each geometrical parameter and checking, for each of its simulations, which is the direction of modification (incremented or reduced) that received more marks.

Let us give a practical example. If we consider the parameter L_2, we can see how in Table 5.5 the simulation $\#L2u$ reflects the variation of Table 5.3 only for the lumped element $R0_t$ (they are both positive) while for simulation $\#L2d$ we can find identical behaviour for the elements $C0_t$ and $K0_{12}$ (again they are all positive). In this case, I choose to refer to $\#L2d$ and to address my research for the final planar EM decreasing the value of L_2 with respect to the initial value. This approach has been adopted for all the parameters and the result of the guidelines is that I have to refer to simulations $\#L1d$, $\#W1d$, $\#L2d$, $\#W2d$ and $\#L3u$. Therefore, this means that I have to look for the optimum layout within

a geometry that has smaller L_1, W_1, L_2, W_2 and bigger L_3.

This advice has been exploited in the run of some guided sweep parameter analysis in CST [2] and results have been used to calculate the sensor tag efficiency (5.6) and to check if its value is really getting close to that 95% expected from the simulated optimization process. Referring to Fig. 5.3a, the best sensor tag is provided by the following final geometrical parameters: $L = 119\,mm$, $L_1 = 80\,mm$, $L_2 = 6\,mm$, $L_3 = 8.5\,mm$, $W = 51\,mm$, $W_1 = 12\,mm$, $W_2 = 5\,mm$, $W_3 = 5\,mm$, $g = 2\,mm$ and $T = 0.075$. In particular, this layout achieves a sensor tag efficiency of about 96.6% using $k = 2$, $\beta_1 = 1$, $\beta_2 = 1$, $\tau_{ref} = 0.9$ and an optimized chip absorbing impedance $Z_{Abs} = (12.1 - j328.7)$ [$Z_{Ref} = (2 - j0.1)$ [4]] within expression (5.6). The final EM sensor tag response calculated at 868 MHz for the optimized chip absorbing impedance $Z_{Abs} = (12.1 - j328.7)$ [$Z_{Ref} = (2 - j0.1)$ [4]] is shown in Fig. 5.15. In this figure it is possible to see a phase shift between the reflection coefficients of the absorbing mode $S_{Abs}(1)$ and $S_{Abs}(2)$ (upward-pointing triangles) of exactly 180° and, also, closely located to the requested $\tau = 0.9$ circle. It is noteworthy also the fact that the modulation efficiency obtained for this configuration is the maximum possible. Indeed, expression (5.5) achieves its maximum when the modulation efficiency for the two considered sensing states has the same value. In this case, the obtained modulation efficiencies are $\eta_1 = \eta_2 = 0.21$.

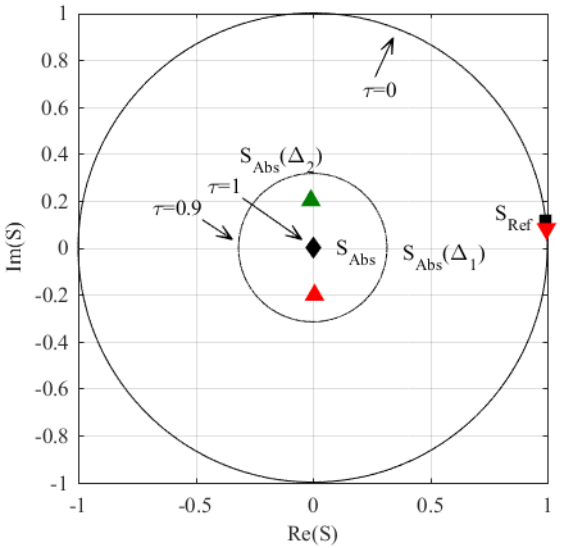

Figure 5.15: Final EM sensor tag response calculated at 868 MHz for the optimized chip absorbing impedance $Z_{Abs} = (12.1 - j328.7)$ [$Z_{Ref} = (2 - j0.1)$ [4]] in comparison with the tag response of a state-of-the-art passive UHF RFID tag (black markers). The reflection coefficients of the absorbing mode $S_{Abs}(1)$ and $S_{Abs}(2)$ are favourably located close to the $\tau = 0.9$ circle and have a phase difference of exactly 180° (upward-pointing triangles). The corresponding reflection coefficients in the reflection mode S_{Ref} lie on the $\tau = 0$ circle (downward-pointing triangles).

Conclusions

In this thesis, I have reported the work and the activities I did during my PhD path, all of them focusing on energy-aware solutions able to reduce or completely avoid the use of battery in portable devices or sensing nodes. In particular, I have proposed a seamless solution to exploit the available PDAs antennas for near-field wireless recharging, with no need for dedicated energy transfer links and charging stations. By choosing a suitable frequency, energy transfer between closely-located portable devices is enabled by exploiting the coupling of their reactive electric field. The proposed solution only needs to equip the portable antennas with a diplexing network, able to decouple the radiation and the power recharging paths. As a proof-of-concept an initial simplified system based on capacitive coupling has been investigated and explained. Based on this initial result, a second full system prototype based on capacitive coupling has been fabricated: the effective coexistence of the two concurrent activities of communication and wireless recharging has been experimentally demonstrated. Of course, this architecture enables WPT with lower efficiency levels than state-of-the-art dedicated resonant reactive links, but it is still sufficient to make the proposed idea a valid, simple and cheap alternative. The proposed theoretical and numerical approach can be further extended to the design of a new generation of mobile antenna system whose layout optimization addresses

at the same time high frequency for far-field and low-frequency near-field performance.

I have also developed an equivalent and simple circuit model of a T-matched dipole that is able to accurately represent the dipole behaviour for several bending states, not only at the nominal RFID operating frequency but also over a 50 MHz band centred around it. This CM model can be used not only for fast evaluation of the antenna sensor tag performance, but also for optimization purpose in order to define the best antenna geometry from the point of view of sensor tag sensitivity with respect to a specific chip impedance.

The presented design method is general and can be adopted for a class of sensor tags (e.g., chipless sensor tag) based on a T-matched dipole. Conversely, the CM of the T-matched dipole in various bending states could be also exploited to design a conventional tag antenna that is insensitive to bending (i.e. $\alpha = 0$).

I have also introduced an innovative figure of merit that has been adopted to drive all the optimization process for finding a final CM that can better reflect the desired performance. At the end of the optimization process, through some retrieved guidelines, it has been shown how to convert the final CM into a final EM that clearly achieves the desired performances when combined with the RFID chip. It is noteworthy that, even if the guidelines are based on a geometrical layout different from the initial planar EM used for demonstrating the whole space mapping technique, the direction of the suggested geometrical parameters modification was correct.

Indeed, five of the six geometrical parameters involved (L_i, W_i with $i = 1, 2, 3$) were correctly addressed. The only suggestion of the whole procedure I consider wrong refers to L_3. In fact, with respect to its initial

value, it wasn't necessary to modify it differently from the guideline that was suggesting to increase it.

In conclusion, it has been shown how the final EM agrees with the expected optimized final CM results in terms of the sensor tag.

Thanks to this, a complete space mapping technique has been described and its feasibility has been proved through a comparison of the sensor tag efficiency between the rough circuit model and the fine electromagnetic model.

Acknowledgements

First of all, I have to thank Prof. Alessandra Costanzo for being my supervisor and for giving me the possibility to explore new fields. In second place, I want to thank Dr. Diego Masotti for his constant and practical support and for introducing me at "teaspoon theory". Apart some misunderstanding during these years, I want to thank them both for showing to me a completely "new world" and for giving to me the opportunity to explore and investigate it.

I want to thank also Prof. Jasmin Grosinger (University of Graz, Austria), my austrian Supervisor, as representative for all the people at IHF in Graz University of Technology that welcome, collaborate and take care of me while I was their guest. The months spent together have been really appreciated and professionally educational. I would also to express my gratitude to the reviewers of my thesis, Prof. Giuseppina Monti (University of Salento, Italy), Prof. Marco Dionigi (University of Perugia, Italy), who provided deep insights and useful remarks.

And now starts the part dedicated to my new friends. All along this period, I shared a lot of experiences with my teammates. As normally it is, not all experiences were nice, but for sure I can affirm that 99% of them were amazing (I can quickly recall Porto, Valence and Kosice). In particular, I shared a lot with my desk-neighbour Marco Fantuzzi, my English friend Massimo Del Prete and "long" dude Alex Pacini. Never-

theless, I want to thank also the other guys of the laboratory. Giacomo Paolini for his always positive point of view. Mazen Al Shanawani for sharing his deep knowledge and different point of view of the world and, not least, taking me back to a swimming-pool. Francesca Benassi for her talkative presence (even if I appreciate her more when she was sitting more far). Marco Zoli for his "alternative" rules of sharing. In addition, I want to thank also all the guys, and ladies, of the surrounding laboratories. In particular, even if I won't specify all the names, I want to thank the current and past people working at Radio Network, Netlab and Biomedical laboratories. Furthermore, apart people already mentioned above, there are many other people that I met during these years within and beyond the academic environment, People that I met, knew and became a friend. Few of them became also something more then a simple friend, while others choose to leave. Nevertheless, even if I won't list them all, a thank for their present or past importance is required.

And now the section dedicated to the relatives and parents.

Giulia, my crazy and artistic cousin. We have been flatmates for more than 4 years and so many things happened during this long period that I cannot mention all of them. We both agree that beginning was a bit hard but, pretty fast, we found an important harmony in terms of each-other understanding.

In the end, but not for importance, I wish to express my heartfelt thanks to my family. Papi, Mamma, Marco, Cecilia, Chiara and Dima: I know that most of the time I was not exactly an "easy person". Nevertheless, you all encouraged and supported me in all my life and, moreover, also all through the academic path and during the doctoral period in Bologna. I wish us to remain tight as we are and, why not, to increase this rare quality for our future.

List of Achievements

Accepted Journal Papers

- M. Del Prete, **F. Berra**, A. Costanzo and D. Masotti, "Seamless Exploitation of Cell-phone Antennas for Near-field WPT by a Frequency-diplexing Approach", in The Institution of Engineering and Technology (IET), November 2016**.**

Accepted Conference Papers

- **F. Berra**, A. Costanzo, M. Dionigi, D. Masotti, F. Mastri, M. Mongiardo and R. Sorrentino, "Antenna design for unified far-field communication and near-field recharging", 2015 9th European Conference on Antennas and Propagation (EuCAP), Lisbon, 2015, pp. 1-4.

- M. Del Prete, **F. Berra**, A. Costanzo and D. Masotti, "Exploitation of a dual-band cell phone antenna for near-field WPT," 2015 IEEE Wireless Power Transfer Conference (WPTC), Boulder, CO, 2015, pp. 1-4.

- G. Paolini, M. Del Prete, **F. Berra**, D. Masotti and A. Costanzo, "An Agile and Accurate Microwave System for Tracking Elderly People Occupancy at Home", in 2016 IEEE MTT-S Latin America

Microwave Conference (LAMC 2016), Puerto Vallarta (MEX), 12-14 Dec. 2016.

- A. Costanzo, D. Masotti, M. Fantuzzi, **F. Berra** and M. Del Prete, "Solutions for Simultaneous Wireless Information and Power Transfer", 2017 International Conference on Electromagnetics in Advanced Applications (ICEAA), Verona (Italy), 2017, pp. 1898-1901.

- **F. Berra**, A. Costanzo, J. Grosinger and L. Görtschacher, "Space mapping design method for an antenna transducer of a bend sensor RFID tag," 2017 47th European Microwave Conference (EuMC), Nuremberg, 2017, pp. 109-112.

Workshops

- **F. Berra**, M. Del Prete, D. Masotti, A. Costanzo, "Dual-band Antenna for simultaneous NF-WPT and FF-communication"; 4th Workshop of the Radio Frequency Engineering Working Group of the Austrian Research Association; Villach (Austria), 18th October 2016

- **F. Berra**, M. Del Prete, D. Masotti, A. Costanzo, "Exploitation of a dual-band cell phone antenna for near-field WPT"; COST IC1301 8th Management Committee, Working Group and Workshop; Kosice (Slovakia), 16th March 2017

- A. Costanzo, D. Masotti, **F. Berra**, M. Del Prete, “Antenna Systems Architectures for Simultaneous Far-Field Communication and Near-Field WPT”, 2017 International Microwave Symposium (IMS), Honolulu (Hawaii), 9th June 2017.

Posters

- M. Fantuzzi, F. Berra, A. Pacini, D. Masotti, F. Mastri, A. Costanzo, "Near-Field WPT to Loosely-Coupled Small Implants", XXI RiNEm Riunione Nazionale di Eletromagnetismo, 12 September 2016, Parma, Italy

Projects

- "European Microwave Week 2014 - Europe's Premier Microwave, RF, Wireless and Radar Event", 8th – 13th October 2014, Rome (Italy) – Workshops & Schortcourses Organization
- "International Spring School on Electromagnetics and emerging technologies for pervasive applications: Internet of Things, Health and Safety", 18th – 20th April 2016, Pontecchio Marconi (Italy) – Organization
- "POR-FESR 2014-2020 - HABITAT: Home Assistance Basata su Internet of Things per l'Autonomia di Tutti", Regione Emilia Romagna (Italy) – Project Proposal and Submission: Accepted

Bibliography

[1] Y. Rahmat-Samii, L. I. Williams, and R. G. Yaccarino, "The UCLA bi-polar planar-near-field antenna-measurement and diagnostics range," *IEEE Antennas and Propagation Magazine*, vol. 37, pp. 16–35, Dec 1995.

[2] CST Microwave Studio 2016, http://www.cst.com/.

[3] NI AWR Design Enviroment, v.10, : http://www.awrcorp.com/.

[4] A. Al-Fuqaha, M. Guizani, M. Mohammadi, M. Aledhari, and M. Ayyash, "Internet of Things: A Survey on Enabling Technologies, Protocols, and Applications," *IEEE Communications Surveys Tutorials*, vol. 17, pp. 2347–2376, June 2015.

[5] Y. Tanabe, T. Chang, A. J. Yeh, and A. S. Y. Poon, "A Small Dual-Band Asymmetric Dipole Antenna for 13.56 MHz Power and 2.45 GHz Data Transmission," *IEEE Antennas and Wireless Propagation Letters*, vol. 13, pp. 1120–1123, 2014.

[6] P. Wu, F. Bai, Q. Xue, X. Liu, and S. Y. R. Hui, "Use of Frequency-Selective Surface for Suppressing Radio-Frequency Interference from Wireless Charging Pads," *IEEE Transactions on Industrial Electronics*, vol. 61, pp. 3969–3977, Aug 2014.

[7] C. Zhu, C. Yu, K. Liu, and R. Ma, "Research on the topology of wireless energy transfer device," in *2008 IEEE Vehicle Power and Propulsion Conference*, pp. 1–5, Sept 2008.

[8] A. Costanzo, M. Dionigi, F. Mastri, M. Mongiardo, J. A. Russer, and P. Russer, "Rigorous network modeling of magnetic-resonant wireless power transfer," *Wireless Power Transfer Journal*, vol. 1, pp. 27–34, 003 2014.

[9] A. Costanzo, M. Dionigi, F. Mastri, M. Mongiardo, J. A. Russer, and P. Russer, "Rigorous design of magnetic-resonant wireless power transfer links realized with two coils," in *2014 44th European Microwave Conference*, pp. 414–417, Oct 2014.

[10] I. Krikidis, S. Timotheou, S. Nikolaou, G. Zheng, D. W. K. Ng, and R. Schober, "Simultaneous wireless information and power transfer in modern communication systems," *IEEE Communications Magazine*, vol. 52, pp. 104–110, Nov 2014.

[11] Q. Chen, K. Ozawa, Q. Yuan, and K. Sawaya, "Antenna Characterization for Wireless Power-Transmission System Using Near-Field Coupling," *IEEE Antennas and Propagation Magazine*, vol. 54, pp. 108–116, Aug 2012.

[12] C. Y. Liou, X. S. Lin, C. H. Tai, and S. G. Mao, "Microwave near-field capacitive coupling system for wireless powering appliations," in *2014 IEEE Wireless Power Transfer Conference*, pp. 56–59, May 2014.

[13] R. D. Fernandes, J. N. Matos, and N. B. Carvalho, "Wireless power transmission based on resonant electrical coupling," in *2014 44th European Microwave Conference*, pp. 17–20, Oct 2014.

[14] M. D. Prete, F. Berra, A. Costanzo, and D. Masotti, "Exploitation of a dual-band cell phone antenna for near-field WPT," in *2015 IEEE Wireless Power Transfer Conference (WPTC)*, pp. 1–4, May 2015.

[15] M. D. Prete, F. Berra, A. Costanzo, and D. Masotti, "Seamless exploitation of cell-phone antennas for near-field wpt by a frequency-diplexing approach," *IET Microwaves, Antennas & Propagation*, November 2016.

[16] T. Sun and X. Xie and Z. Wang, *Wireless Power Transfer for Medical Microsystems*. Springer, 2013.

[17] N. Shinohara, *Wireless Power Transfer via Radiowaves*. Wiley, 2014.

[18] A. Gopinath, "All About Transferring Power Wirelessly," *Electronics for You E-zine - EFY Enterprises Pvt. Ltd.*, pp. 52–56, Aug 2013.

[19] X. Lu, P. Wang, D. Niyato, D. I. Kim, and Z. Han, "Wireless charging technologies: Fundamentals, standards, and network applications," *IEEE Communications Surveys Tutorials*, vol. 18, pp. 1413–1452, Nov 2016.

[20] A. Costanzo and D. Masotti, "Energizing 5g: Near- and far-field wireless energy and data trantransfer as an enabling technology for the 5g iot," *IEEE Microwave Magazine*, vol. 18, pp. 125–136, May 2017.

[21] D. Masotti, A. Costanzo, M. D. Prete, and V. Rizzoli, "Time-modulation of linear arrays for real-time reconfigurable wireless

power transmission," *IEEE Transactions on Microwave Theory and Techniques*, vol. 64, pp. 331–342, Feb 2016.

[22] S. Mao, J. Zhang, K. Song, G. Wei, and C. Zhu, "Wireless power transfer using a field-enhancing coil and a small-sized receiver with low coupling coefficient," *IET Power Electronics*, vol. 9, no. 7, pp. 1546–1552, 2016.

[23] M. Nariman, F. Shirinfar, A. P. Toda, S. Pamarti, A. Rofougaran, and F. D. Flaviis, "A compact 60-ghz wireless power transfer system," *IEEE Transactions on Microwave Theory and Techniques*, vol. 64, pp. 2664–2677, Aug 2016.

[24] K. F. Warnick, R. B. Gottula, S. Shrestha, and J. Smith, "Optimizing power transfer efficiency and bandwidth for near field communication systems," *IEEE Transactions on Antennas and Propagation*, vol. 61, pp. 927–933, Feb 2013.

[25] E. Sazonov and M. Neuman, *Wearable Sensors: Fundamentals, Implementation and Applications.* Academic Press, 2014.

[26] C. A. Balanis, "Antenna theory: a review," *Proceedings of the IEEE*, vol. 80, pp. 7–23, Jan 1992.

[27] C. A. Balanis, *Antenna Theory Analysis and Design.* Wiley, 2005.

[28] N. Tesla, "Apparatus for transmitting electrical energy", U.S. patent number 1119732A, issued in December 1914.

[29] A. Kurs, A. Karalis, R. Moffatt, J. D. Joannopoulos, P. Fisher, and M. Soljacic, "Wireless power transfer via strongly coupled magnetic resonances," *Science*, vol. 317, pp. 83–86, July 2007.

[30] O. Jonah and S. V. Georgakopoulos, "Wireless power transfer in concrete via strongly coupled magnetic resonance," *IEEE Transactions on Antennas and Propagation*, vol. 61, pp. 1378–1384, March 2013.

[31] H. Hu and S. V. Georgakopoulos, "Wireless power transfer in human tissue via conformal strongly coupled magnetic resonance," in *2015 IEEE Wireless Power Transfer Conference (WPTC)*, pp. 1–4, May 2015.

[32] Y. Su, C. Tang, S. Wu, and Y. Sun, "Research of lcl resonant inverter in wireless power transfer system," in *2006 International Conference on Power System Technology*, pp. 1–6, Oct 2006.

[33] T. Linlin, H. Xueliang, L. Hui, and H. Hui, "Study of wireless power transfer system through strongly coupled resonances," in *2010 International Conference on Electrical and Control Engineering*, pp. 4275–4278, June 2010.

[34] W. X. Chen and Q. H. Chen, "Application of class-e converter in magnetic resonant wpt system," in *2016 IEEE International Conference on Aircraft Utility Systems (AUS)*, pp. 320–324, Oct 2016.

[35] H. Qi, W. Chen, Y. Sha, Y. Han, H. Li, and X. Yang, "High frequency conducted emi modeling of a series-series resonant wpt system," in *2017 IEEE 3rd International Future Energy Electronics Conference and ECCE Asia (IFEEC 2017 - ECCE Asia)*, pp. 2279–2282, June 2017.

[36] V. Stanimir, E. Baikova, and J. Luis, "Electromagnetic field as the wireless transporter of energy," *Facta universitatis - series: Electronics and Energetics*, vol. 25, pp. 171–181, Jan 2012.

[37] M. Huschens, "Various techniques for wireless charging," *EE Times-Asia*, pp. 1–4, Jan 2015.

[38] S. Moulali and K. Subbarao, "A review on recent developments in wireless power transfer," *International Journal of Circuit Theory and Applications*, vol. 10, pp. 421–426, 1 2017.

[39] A. Karalis, J. Joannopoulos, and M. Soljačiĉ, "Efficient wireless non-radiative mid-range energy transfer," *Annals of Physics*, vol. 323, pp. 34–48, Jan 2008.

[40] B. Lenaerts and R. Puers, *Omnidirectional Inductive Powering for Biomedical Implants*. Springer, 2009.

[41] Murata Manufacturing, "World's first!! Production starts for Capacitive Coupling Wireless Power Transmission Module," *ECN magazine. Advantage Business Media*, pp. 1–4, Oct 2011.

[42] Muhannad S. Bakir and James D. Meindl, *Integrated Interconnect Technologies for 3D Nanoelectronic Systems*. Artech House, 2008.

[43] H. Kenichi, "Wireless Power Transmission at Rotating and Sliding Elements by Using the Capacitive Coupling Technology", in *2014 ANSYS Electronic Simulation Expo October 9-10*, Tokyo, Oct 2014.

[44] N. Liu, "Coupling games in metamaterials," *Physik Journal*, pp. 57–60, Sep 2010.

[45] P. Camurati and H. Bondar, "Device for transporting energy by partial influence through a dielectric medium", U.S. patent number 20090206675A1, issued in March 2009.

[46] A. Costanzo, M. Dionigi, D. Masotti, M. Mongiardo, G. Monti, L. Tarricone, and R. Sorrentino, "Electromagnetic Energy Harvest-

ing and Wireless Power Transmission: A Unified Approach," *Proceedings of the IEEE*, vol. 102, pp. 1692–1711, Nov 2014.

[47] T. S. Bird, N. Rypkema, and K. W. Smart, "Antenna impedance matching for maximum power transfer in wireless sensor networks," in *2009 IEEE Sensors*, pp. 916–919, Oct 2009.

[48] M. Zargham and P. G. Gulak, "Maximum Achievable Efficiency in Near-Field Coupled Power-Transfer Systems," *IEEE Transactions on Biomedical Circuits and Systems*, vol. 6, pp. 228–245, June 2012.

[49] CST Microwave Studio 2013, http://www.cst.com/.

[50] D. Masotti and A. Costanzo, "Time-based rf showers for energy-aware power transmission," in *2017 11th European Conference on Antennas and Propagation (EUCAP)*, pp. 783–787, March 2017.

[51] A. Costanzo, D. Masotti, M. Fantuzzi, and M. D. Prete, "Co-design strategies for energy-efficient uwb and uhf wireless systems," *IEEE Transactions on Microwave Theory and Techniques*, vol. 65, pp. 1852–1863, May 2017.

[52] A. Costanzo, F. Mastri, M. Dionigi, and M. Mongiardo, "Wireless resonant-type power transfer links with relay elements: Harmonic balance design," in *2012 42nd European Microwave Conference*, pp. 225–228, Oct 2012.

[53] F. Berra, A. Costanzo, M. Dionigi, D. Masotti, F. Mastri, M. Mongiardo, and R. Sorrentino, "Antenna design for unified far-field communication and near-field recharging," in *2015 9th European Conference on Antennas and Propagation (EuCAP)*, pp. 1–4, May 2015.

[54] S. L. Zuo, Z. Y. Zhang, and J. J. Xie, "Design of dual-monopole slots antenna integrated with monopole strip for wireless wide area network mobile handset," *IET Microwaves, Antennas Propagation*, vol. 8, pp. 194–199, February 2014.

[55] D. G. Kang and Y. Sung, "Compact Hexaband PIFA Antenna for Mobile Handset Applications," *IEEE Antennas and Wireless Propagation Letters*, vol. 9, pp. 1127–1130, 2010.

[56] A. Friedrich, B. Geck, O. Klemp, and H. Kellermann, "On the design of a 3D LTE antenna for automotive applications based on MID technology," in *2013 European Microwave Conference*, pp. 640–643, Oct 2013.

[57] G. Augustin, B. P. Chacko, and T. A. Denidni, "Uniplanar folded monopole antenna for mobile phone applications in LTE/GSM/UMTS/WiFi band," in *2014 IEEE Antennas and Propagation Society International Symposium (APSURSI)*, pp. 388–389, July 2014.

[58] ADS Keysight software 2015, http://www.keysight.com/.

[59] D. Masotti, A. Costanzo, M. D. Prete, and V. Rizzoli, "Genetic-based design of a tetra-band high-efficiency radio-frequency energy harvesting system," *IET Microwaves, Antennas Propagation*, vol. 7, pp. 1254–1263, December 2013.

[60] M. Fantuzzi, M. Rajabi, G. Avolio, A. Costanzo, and D. Schreurs, "Large signal rectifier characterization for simultaneous data and Power Transfer," in *2016 IEEE Wireless Power Transfer Conference (WPTC)*, pp. 1–4, May 2016.

[61] K. Moussakhani, R. K. Amineh, and N. K. Nikolova, "Estimating the Efficiency of Antennas Used as Sensors in Microwave Tissue Measurements," *IEEE Transactions on Antennas and Propagation*, vol. 62, pp. 295–301, Jan 2014.

[62] MATLAB R2017a, The MathWorks Inc., Natick, MA, 2017.

[63] D. A. Frickey, "Conversions between S, Z, Y, H, ABCD, and T parameters which are valid for complex source and load impedances," *IEEE Transactions on Microwave Theory and Techniques*, vol. 42, pp. 205–211, Feb 1994.

[64] R. B. Marks, D. F. Williams, and D. A. Frickey, "Comments on "Conversions between S, Z, Y, h, ABCD, and T parameters which are valid for complex source and load impedances" [with reply]," *IEEE Transactions on Microwave Theory and Techniques*, vol. 43, pp. 914–915, April 1995.

[65] L. Smerklo, Y. Kempa, Y. Rybak, V. Rybak, Z. Dufanets, and V. Hnativ, "UHF Transceiver," in *2006 International Conference - Modern Problems of Radio Engineering, Telecommunications, and Computer Science*, pp. 561–561, Feb 2006.

[66] C. Occhiuzzi, S. Caizzone, and G. Marrocco, "Passive UHF RFID antennas for sensing applications: Principles, methods, and classifcations," *IEEE Antennas and Propagation Magazine*, vol. 55, pp. 14–34, Dec 2013.

[67] S. Capdevila, L. Jofre, J. Romeu, and J. C. Bolomey, "Passive RFID based sensing," in *2011 IEEE International Conference on RFID-Technologies and Applications*, pp. 507–512, Sept 2011.

[68] J. Grosinger, L. Görtschacher, and W. Bösch, "Passive RFID Sensor Tag Concept and Prototype Exploiting a Full Control of Amplitude and Phase of the Tag Signal," *IEEE Transactions on Microwave Theory and Techniques*, vol. 64, pp. 4752–4762, Dec 2016.

[69] M. Ghassemi, M. Bakr, and N. Sangary, "Antenna design exploiting adjoint sensitivity-based geometry evolution," *IET Microwaves, Antennas Propagation*, vol. 7, pp. 268–276, March 2013.

[70] S. Koziel and S. Ogurtsov, *Antenna Design by Simulation-Driven Optimization. Surrogate-Based Approach.* Springer, 2014.

[71] J. W. Bandler, R. M. Biernacki, S. H. Chen, P. A. Grobelny, and R. H. Hemmers, "Space mapping technique for electromagnetic optimization," *IEEE Transactions on Microwave Theory and Techniques*, vol. 42, pp. 2536–2544, Dec 1994.

[72] V. Rizzoli, A. Costanzo, D. Masotti, A. Lipparini, and F. Mastri, "Computer-aided optimization of nonlinear microwave circuits with the aid of electromagnetic simulation," *IEEE Transactions on Microwave Theory and Techniques*, vol. 52, pp. 362–377, Jan 2004.

[73] X. Yi, C. Cho, J. Cooper, Y. Wang, M. Tentzeris, and R. Leon, "Passive wireless antenna sensor for strain and crack sensing - Electromagnetic modeling, simulation, and testing," *Smart Materials and Structures*, vol. 22, no. 8, 2013.

[74] D. Masotti, M. Fantuzzi, and A. Costanzo, "Next generation zero-power RFID-tag for UWB pervasive identification," in *2016 IEEE International Smart Cities Conference (ISC2)*, pp. 1–4, Sept 2016.

[75] G. Marrocco, "The art of UHF RFID antenna design: impedance-matching and size-reduction techniques," *IEEE Antennas and Propagation Magazine*, vol. 50, pp. 66–79, Feb 2008.

[76] K. Kurokawa, "Power Waves and the Scattering Matrix," *IEEE Transactions on Microwave Theory and Techniques*, vol. 13, pp. 194–202, Mar 1965.

[77] B. Rembold, "Optimum modulation efficiency and sideband backscatter power response of rfid-tags," *Frequenz*, vol. 63, pp. 9–13, Jan 2009.

[78] Impinj Inc., "Monza X-2K RFID Dura Chips" [Online]. Available: https://support.impinj.com/hc/en-us/articles/202756848-Monza-X-2K-Dura-Datasheet.pdf [Revised March 2014].